UNIVERSITY OF GHANA

COLLEGE BASIC AND APPLIED SCIENCES

CHARACTERIZATION OF FLEXIBLE ORGANIC-INORGANIC PHOTOVOLTAIC DEVICE MATERIAL

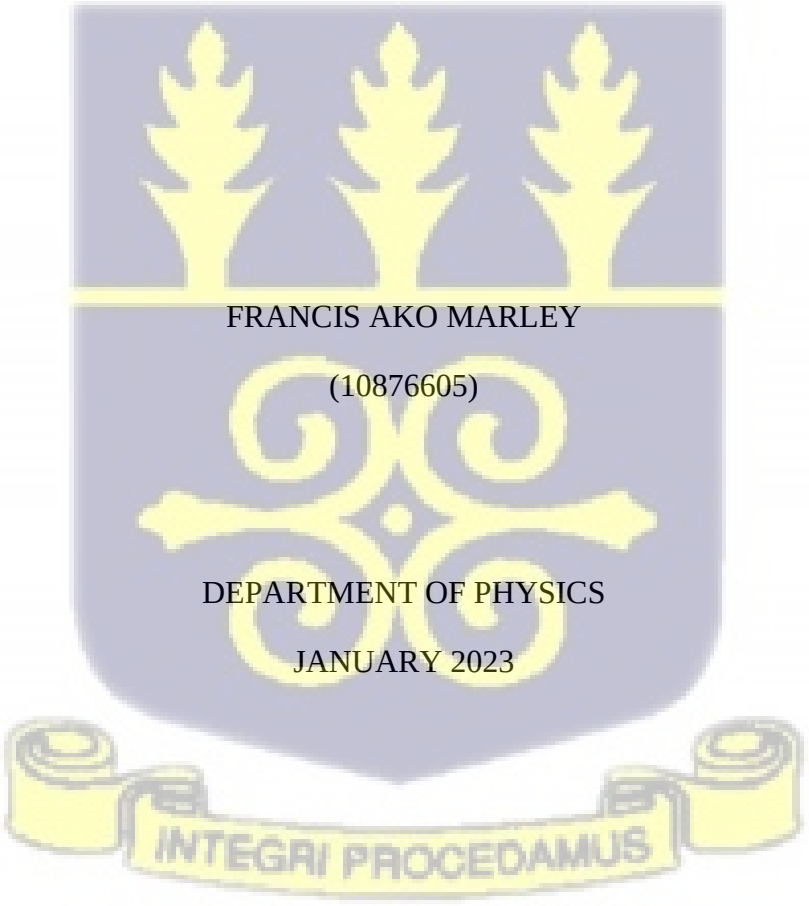

FRANCIS AKO MARLEY

(10876605)

DEPARTMENT OF PHYSICS

JANUARY 2023

UNIVERSITY OF GHANA

COLLEGE BASIC AND APPLIED SCIENCES

CHARACTERIZATION OF FLEXIBLE ORGANIC-INORGANIC PHOTOVOLTAIC DEVICE MATERIAL

BY

FRANCIS AKO MARLEY

(10876605)

THIS THESIS IS SUBMITTED TO THE UNIVERSITY OF GHANA, LEGON, IN PARTIAL FULFILLMENT OF THE REQUIREMENT FOR THE AWARD OF **MPHIL IN PHYSICS DEGREE**

DEPARTMENT OF PHYSICS

JANUARY 2023

DECLARATION

I, Francis Ako Marley (10876605), hereby declare that this work was carried out by me under the supervision of Dr. Joseph Asare and Dr. George Nkrumah-Buandoh, and that no previous submission on this topic has been made to this university or any other institution. Related works by others have been duly acknowledged by reference to the author.

…… 10/02/2023 ……

FRANCIS AKO MARLEY DATE

(STUDENT)

…… 10/02/2023 ……

DR. JOSEPH ASARE DATE

(SUPERVISOR)

…… 10/02/2023 ……

DR. GEORGE NKRUMAH-BUANDOH DATE

(CO. SUPERVISOR)

ACKNOWLEDGEMENTS

I would like to express my profound gratitude to Dr. Joseph Asare and Dr George Nkrumah-Buandoh for their immense contributions and guidance towards the success of this work. I would like to extend my gratitude to Dr. Nicola Serani (ICTP, Italy) and Dr. Gebreyesus Hagoss for their guidance and explanations during the first-principle study. My appreciation also goes to Dr. Daniel Sekyi-Arthur for the numerous discussions held pertaining to this work. Moreover, I would like to acknowledge my family, friends and colleagues for their love and support during this research. I finally want to thank the almighty God for the opportunity to work with these wonderful people.

TABLE OF CONTENT

LIST OF FIGURES

LIST OF TABLES

ABSTRACT

Presented is the results of a study using density functional theory of the electrical characteristics of copper-doped nickel (Cu:NiO) and nickel oxide (NiO), and their performances when utilized as Hole Transport Layer (HTL) in photovoltaic (PV) devices by modelling their I-V characteristics is presented. From first-principle it was observed that, doping NiO with a Cu ion introduced more states in the valence band enhancing the charge transport property of the material. The band gap of NiO reduced from 3.04 eV to 2.63 eV in the unstable supercell structure of Cu:NiO and then to 1.65 eV in the stable supercell structure of Cu:NiO. The defect created by the substitution of Cu ion for Ni ion appears to have given rise to additional electronic states near the bandgap which increases the conductivity of holes substantially. Both stable and unstable supercell structures of Cu:NiO showed a direct band gap which eases the transition of holes from the active layer to the HTL. There was also a shift in Fermi level towards the valence band in both stable and unstable supercell structures thus enhancing hole mobility in the HTL. The unstable Cu:NiO showed the highest efficiencies when used as a composite HTL with poly(3,4-ethylenedioxythiophene) polystyrene sulfonate (PEDOT:PSS) as compared to PEDOT:PSS/NiO, PEDOT:PSS and PEDOT:PSS/Cu:NiO (stable). This demonstrates how the HTL enhances device performance in applications for organic-inorganic electronic devices and provides a better knowledge of its electrical characteristics.

CHAPTER 1

1.1 Background

Photovoltaic is the generation of voltage between two electrodes when light is incident on a semiconductor material, either solid or liquid, when placed between the two electrodes [1]. Looking at the photosynthetic process one can understand where the inspiration to harness energy from the sun for daily consumption came from. Solar energy is absorbed by the photosynthetic mechanism in the plant using pigments known as chlorophyll [2], the absorbed energy leads to the break-down of water and fixing of carbon dioxide to produce organic sugars and oxygen for daily consumption [3]. In 1839, Alexandre-Edmond Becquerel was the first to demonstrate the photovoltaic effect using an electrolyte solution. He observed that electricity was generated when he coated the electrodes with light-sensitive materials such as AgCl or AgBr and were exposed to a light source [4]. The photoconductive nature of selenium was the next promising anomaly to be observed by Adams and Day [5]. Their experiment showed that the photovoltaic effect could be observed in an all-solid-state system. At that time, the notion of harnessing electrical energy from the sun was still alien to most scientists. In 1905, Albert Einstein in his paper "On a Heuristic Point of View Concerning the Production and Transformation of Light" [6], provided the theoretical basis for the photoelectric effect. For that finding, he was awarded the Noble Prize in Physics, which further raised awareness of the process of turning light energy into electrical energy. A few years after Adams and Day made their discovery, Charles Fritts constructed the first photovoltaic cell using selenium, which generated electricity from the sunlight in New York [4]. As good as the invention was, it had a major problem, and it was that, the photovoltaic cell was only able to convert less than 0.5% of the sunlight to electricity. A significant breakthrough was achieved in solar cell technology when in the 1950s, Gerald Pearson, Darryl Chapin, and Calvin Fuller [7],

invented the first silicon-based photovoltaic cell, that operated at an efficiency of 5.7%, ten times more efficient than the one created by Charles Fritts, at the Bell Telephone Laboratories in New Jersey [8]. This led to the application of photovoltaics in space technology when the first PV-powered satellite, Vanguard was launched in March 1958 [9]. The efficiency of silicon-based solar cells has been boosted from 5.7% [10] in the 1950s to ~30% in 2020 [11] which has reached the theoretical maximum efficiency for a silicon-based PV cell of 30% predicted by Shockley and Queisser in 1961 [12].

1.2 Generations of Photovoltaic Cells

To understand the various types of PVs that exist to date, it will be best to categorize them into generations [13]. The generations of PV cells essentially elucidate the phases by which they have evolved to date. Currently, there are four (4) generations of solar PVs and each generation has its unique features and properties that distinguish them from each other [14]. The first generation entails polycrystalline and monocrystalline silicon including gallium arsenide (GaAs). The only available PV cell technology for this generation is based on crystalline silicon. Thin-film solar PV cells made of microcrystalline silicon (c-Si) and amorphous silicon are included in the second generation. This generation also includes cadmium telluride (CdTe) or cadmium sulfide (CdS), copper indium gallium selenide (CIGS), and cadmium telluride. The third generation of PV cells comprises organic polymer-based PV cells, dyed-sensitized cells, perovskites, and nanocrystalline film-based technologies like quantum dots. The fourth generation, which is currently being developed, combines the stability of modern inorganic nanostructures with flexible and inexpensive thin-film polymers. This generation generally involves organic-inorganic PV cells.

1.2.1 First-generation PV cells

Ninety percent of the global market for PV energy is made up of monocrystalline and polycrystalline silicon. [15]. Raw silicon is abundant on the earth and therefore not expensive to acquire. The main challenge faced with silicon is that it naturally exists in oxide form, silicon dioxide (SiO_2), hence, high energy input is needed to extract pure silicon crystals for PV applications. Monocrystalline silicon is the earliest PV technology to exist and presently has an efficiency of about ~28% under laboratory conditions [11]. The efficiency drops by a little for commercial PV cells to values between 15-22% [15]. The manufacturing process is the principal contributor to the fluctuation of efficiency in these cells. The Czochralski process, created by Jan Czochralski in 1916, is used in the fabrication of monocrystalline silicon cells with a purity of 99.9999% silicon [16]. Because pure silicon has poor electrical conduction, small amounts of impurities like boron or phosphorous are added to it to increase its electrical conduction ability[17]. Depending on the material it is doped with, silicon can either become n- or p-type. For instance, adding boron to silicon results in a p-type semiconductor, but adding phosphorus results in an n-type semiconductor.

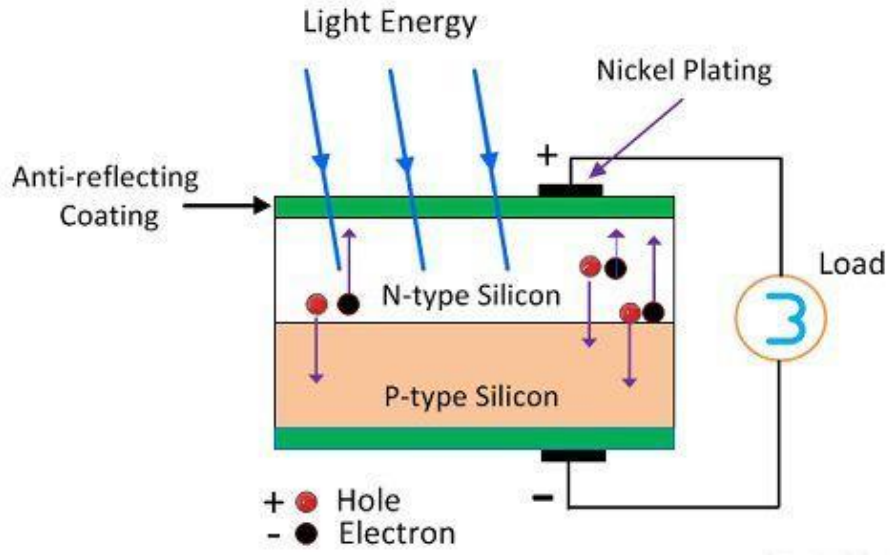

Figure 1.1: Schematic diagram of Monocrystalline PV module.

Compared to monocrystalline PVs, polycrystalline PVs have a relatively low cost of production by use of the block smelting fabrication method. The stage for the formation of the ingot [15] is not required for this method. The first efficiency of this PV module was recorded in 1984, with values below 15% under laboratory conditions [18]. Due to their expensive production method, which is still a hurdle for the industry, first-generation PVs are quite expensive.

1.2.2 Second-generation PV cells

Thin-film PV cells are less expensive, flexible, and thinner compared to first-generation PVs. The active layers of first-generation PV cells which were in the range of 200-300µm are now 10µm in second-generation PVs [19]. Due to their thinner layers, more impurities can be added since the charges do not have to travel long a distance in the device. Thin films are processed and deposited at low temperatures compared to crystalline silicon which requires high temperatures for manufacturing. Minimal active layer volume, low processing temperatures, and high purity are some of the advantages that contribute to the low cost per area for thin-film PV cells, however,

they come at the expense of low efficiency relative to crystalline silicon. The most commonly used materials for inorganic thin-film PV cells are cadmium telluride (CdTe), amorphous silicon (a-Si), and copper indium gallium selenide, $Cu(InGa)Se_2$ [20].

With the increasing production of thin-film PV cells, there are still challenges that are associated with this generation of PV cells. While thin-film PVs address each of these tasks as a separate operation, crystalline PV cells have had plenty of time to explore and create creative ways to improve silicon purity, wafer fabrication, cell processing, and encapsulation. Copper indium gallium selenide (CIGS) faces a long-term issue with the limited amount of indium reserves available. Cadmium is also toxic to the environment and therefore is a huge concern for CdTe PV cells.

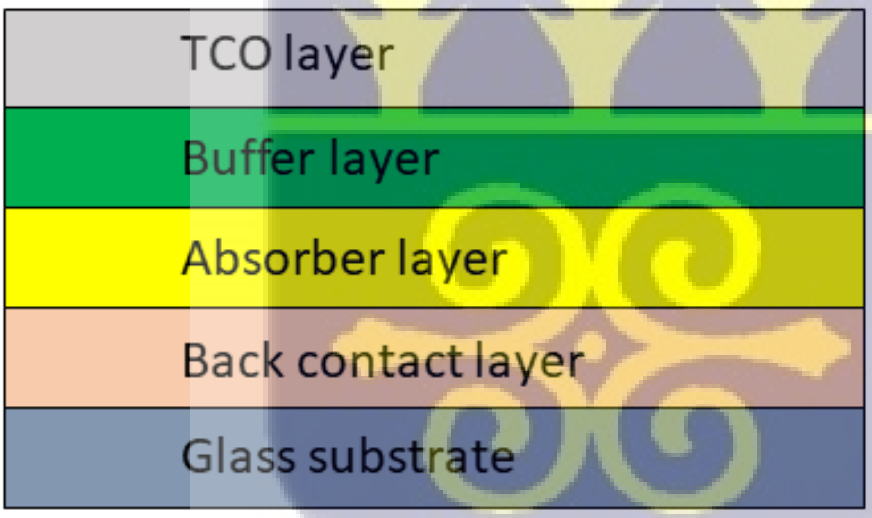

Figure 1.2: A schematic diagram of a typical CIGS PV cell.

1.2.3 Third-generation PV cells

A dye-sensitized PV cell has shown to be a very affordable PV cell and is a member of the class of solar thin-film cells [21]. A photo-sensitized anode, a photo electro-chemical system, and an

electrolyte are used to make it [22]. The dye-sensitized PV, commonly referred to as the Gratzel cell, has a variety of unique characteristics, including the ability to easily adapt to the traditional roll-printing technique and the provision of varied ranges via its semi-translucent property, which enables the use of glass-based systems [23], [24].

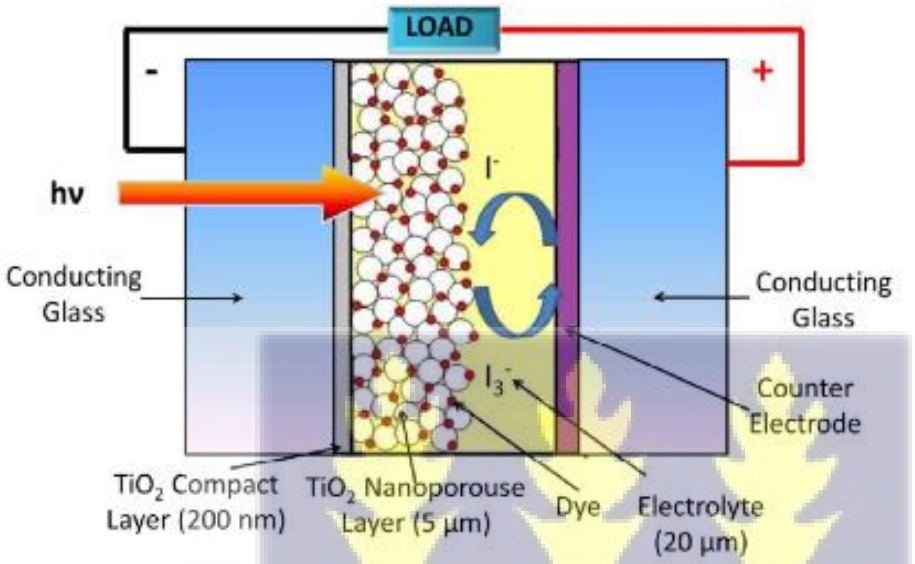

Figure 1.3: The structure of a dye-sensitized PV cell [25].

On the other side, quantum dots utilise the dots as an absorbing PV substance. Materials like Si, CISGS, or CdTe [26] are replaced in this method. By changing the size of the dots, the bandgap of the dots may be varied to a wide variety of energy levels. As a result, quantum dots are desirable for multi-intersection solar-powered PV cells to enhance the absorption of various sunlight spectra [27], [28]. The quantum dot's energy bandgap widens as its size shrinks.

1.2.4 Fourth-generation PV cells

To achieve flexibility and maintain integrity throughout the device, all the layers such as semiconductor materials, dielectric layers, and electrodes must be compliant to a flexible substrate [29]. Nanowires are classified into three types; inorganic, organic, and metal oxide nanowires [30].

Most commonly used flexible conductor materials as electrodes are silver nanowires [31], graphene [32], carbon nanotubes [33], and conductive polymer [34]. The aforementioned electrodes can theoretically be used with any flexible electronic device however it is important to note that some semiconductor-electrode pairs will provide different results than others, therefore it is preferable to choose electrodes that are compatible with the device. The class of 1D nanostructures currently includes nanowires as a significant component, which offers a way to clarify the interaction between optical, charge transport, and other features with dimensionality and size constraints [35].

1.3 Photovoltaic Device Performance Parameters

Both organic and inorganic PV cells have properties of current density J vs. voltage V that, when measured in the dark, resemble the exponential response of a diode with a large forward bias current and a modest reverse bias current. The J-V characteristics under irradiance are the superposition of the photocurrent and the dark J-V characteristics. When light is incident on a PV device, a photocurrent is created in the device along with the diode behavior. The following is the Shockley equation for the J-V characteristics of a perfect PV device:

$$J = J_0 \left[exp\left(\frac{eV}{nkT}\right) - 1 \right] - J_{ph} \qquad 1.1.1$$

Where J is the current density, J_0 is the reverse saturation current, J_{ph} is an additional photocurrent term [36], e is the elementary charge, V is the applied voltage, n is the ideality factor, k is the Boltzmann constant, and T is the temperature [37].

1.3.1 Open-circuit voltage

The potential difference across a cell when a PV device is open-circuited, $J = 0$, is referred to as the open-circuit voltage, V_{OC}. No power can be produced at this voltage since power is the consequence of current and voltage. The V_{OC}, can be thought of as the situation where the generation of photocurrent and dark current processes balance one another.

1.3.2 Short-circuit current

Short-circuit current density J_{SC} is the current density at the instance when $V = 0$, which is the same as connecting the PV device's two electrodes together or short-circuiting it. Again, similar to V_{OC} power is not produced at this point, but J_{SC} serves as the benchmark for power generation. For ideal PV cells J_{SC} is equal to the photocurrent density J_{ph}.

1.3.3 Fill-factor

While J_{SC} and V_{OC} specify the boundaries of power generation in a PV cell, the product of the maximum voltage V_{Max} and maximum current density J_{Max} will give the maximum power density produced P_{Max}. Due to resistance, recombination losses, and diode behavior, $|J_{Max}| \times V_{Max}$ are always less than $|J_{SC}| \times V_{OC}$, respectively. The fill-factor describes the ratio between them and is given by:

$$FF = \frac{J_{Max}\, V_{Max}}{J_{SC}\, V_{OC}} \qquad 1.1.2$$

FF indicates how close J_{Max} and V_{Max} come to J_{SC} and V_{OC}, which are the boundaries of power production. It is necessary to note that the value of FF is directly proportional to P_{Max}, therefore higher FF will result in higher P_{Max}.

1.3.4 Power Conversion Efficiency (PCE)

Power conversion efficiency η is the most talked-about performance parameter of a PV cell and is defined as the percentage of how much incident irradiance I_L [38] is converted to output power. The load determines the power output, therefore, depending on the load, the operation point of the PV cell on the J-V curve also changes. The equation for calculating PCE is expressed as:

$$\eta = \frac{|J_{Max}| \times V_{Max}}{I_L} \times 100\% = \frac{FF \times |J_{SC}| \times V_{OC}}{I_L} \times 100\% \qquad 1.1.3$$

This depicts that the values of FF, J_{SC}, and V_{OC} affect η directly. Power conversion efficiency is crucial to the study of PV cells because it determines how well a PV cell's surface area is being utilized and how much PV cell surface area is needed to create a specified amount of power [39].

1.5 Motivation

The properties of the materials used to make a photovoltaic device have an impact on how efficient it is. These properties include the band gap of the various materials, carrier lifetime and carrier mobility which translate into the charge transport property. In understanding the charge transport properties, steps can be taken to optimize the PV device design to improve efficiency. Characterizing charge transport can further aid in identifying potential bottlenecks that may be limiting device performance.

1.6 Problem statement

The efficiency of flexible photovoltaic devices relies heavily on the performance of the hole transport layer, a critical component responsible for the efficient extraction and transport of holes from the light-absorbing layer to the electrode. To optimize the design and performance of photovoltaic devices, it is essential to comprehensively characterize the HTL material, as variations in material properties can significantly impact device performance. This research aims to computational investigate and characterize the HTL material properties, including energy band gaps, density of states, current-voltage characteristics, and power conversion efficiency, to gain deeper insights into its impact on device performance. The findings of this study will contribute to the development of more efficient and stable photovoltaic devices, ultimately advancing the field of renewable energy technology.

1.7 Aim & Objectives

This work seeks to elucidate the role of copper-doped nickel oxide when used as a composite layer for in an organic-inorganic PV device. In this investigation, the following will be achieved:

- The band gap and density of states of NiO and Cu:NiO will be modelled from first principle using density functional theorem.
- The current-voltage characteristics as well as the efficiencies of the doped and undoped composite HTL in the PV structure would be investigated using a solar cell simulator.

1.8 Scope of work

Chapter 1 presents a background of the research and discusses the various generations of PV devices that has led to the improvement of the optoelectronic properties of thin-film PV at low cost bringing about the motivation for this research.

Chapter 2 discusses the factors that affect carrier charge transport properties in the HTL and how they contribute to the performance of a PV device. The factors considered include: charge mobility of the material, temperature, doping, electric fields and the crystal structure of the material. At the end, computational methods of characterizing charge transport would be discussed with the focus on density functional theory and the continuity equation for PV cells.

Chapter 3 describes the methods used in characterizing charge transport computationally. Relaxation of the crystal system of the material, a self-consistent field calculation, a Hubbard correction and a non-self-consistent field calculation were also discussed in this chapter. The chapter further takes a look at device performance simulation of hole transport layers incorporated into a PV cell configuration.

Chapter 4 reports the results of the computational simulations which include the band structures, the density of states and the I-V characteristics of the materials. The efficiencies of the PV devices with the different hole transport layers were compared. The implication of the findings of the work were discussed.

Chapter 5 entails the conclusions made from the research concerning the aims of the study. This chapter also highlights some recommendations that can be done in the future with regards to this work to explore further research avenues to optimize the optoelectronic properties of the HTL.

CHAPTER 2

In this part, a review of the factors that affect charge carrier transport in materials for PV applications is presented. These factors include, charge mobility in the material, temperature, doping, electric fields and the crystal structure of the material. Moreover, various computational methods of charge transport characterization in PVs are discussed.

2.1 Charge Transport

Charge transport refers to the movement of charge carriers through a material or device [40]. This occurs through the motion of electrons or holes due to thermal excitations or application of an electric field. The study of charge transport in PV devices is very important as it is closely linked to the optoelectronic properties of the device.

With a valence band and a conduction band that are separated by an energy band gap, the band model [41], [42] applied in traditional semiconductor theory is used to describe charge transport. Excitation of electrons from the valence band to the conduction band causes electrical conduction in the material. Due to their chemical makeup, organic semiconductors have the highest occupied molecular orbital (HOMO) and lowest unoccupied molecular orbital (LUMO). The valence band and conduction band are analogs of the HOMO and LUMO, respectively [43], [44]. When electrons absorb a photon, they are excited from the HOMO to the LUMO. A descriptive picture of charge transport in organic PV materials is that of localized charge hopping between sites. A network of sites is distributed in space and energy, as displayed in Figure 2.1. Charges move from one site to another by thermally activated hopping or by tunnelling [45]–[47].

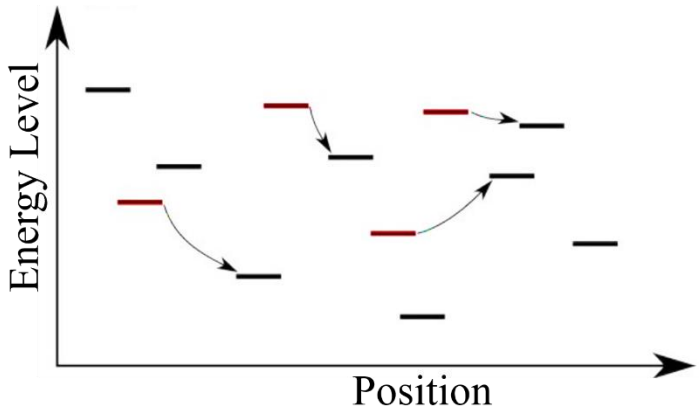

Figure 2.1: The hopping model of charge carriers occupying sites with their movements indicated by the arrows.

2.2 Types of Charge Transport

Charge transport can be classified into two types namely, normal charge transport and dispersive charge transport [48]. In normal charge transport, the charge carriers move through a material in a non-dispersive manner, meaning that their motion is not influenced by the energy of the carriers. This type of transport occurs in materials with a single, well-defined bandgap and a single type of carrier.

On the other hand, in dispersive charge transport, the charge carriers' motion is influenced by their energy. This can occur in materials with multiple bands or multiple types of carriers, such as in a semiconductor with both electrons and holes. Charge carriers with different energies will experience different scattering rates and mobility, leading to a dispersive transport of charge.

The hopping model depicts that charge transport is a consequence of the chaotic movement of charges throughout a complex spatial and energetic landscape. At the microscopic level, some charge carriers may follow a fortunate sequence of jumps and make quick motions through the

film, while others might take quite longer [49]. Some charge carriers move faster than others at any given time, hence, the classical description of carrier mobility is not complete which means charge carrier mobility can no longer be regarded as an invariant material property [48], [50]–[53].

Dispersive transport happens when the photocurrent declines with time even before any charge carriers are extracted. The photocurrent is as a result of the average motion of all carriers, so this means that the average velocity is decreasing and the number of carriers is decreasing. This time-dependent mobility makes it challenging to extract a sufficient amount of charge carriers, resulting in a thickness-dependence, where thicker devices have longer distances for charge carriers to transit eventually allowing more time for the photocurrent to decay unlike that of the normal charge transport as shown in Figure 2.2 [48].

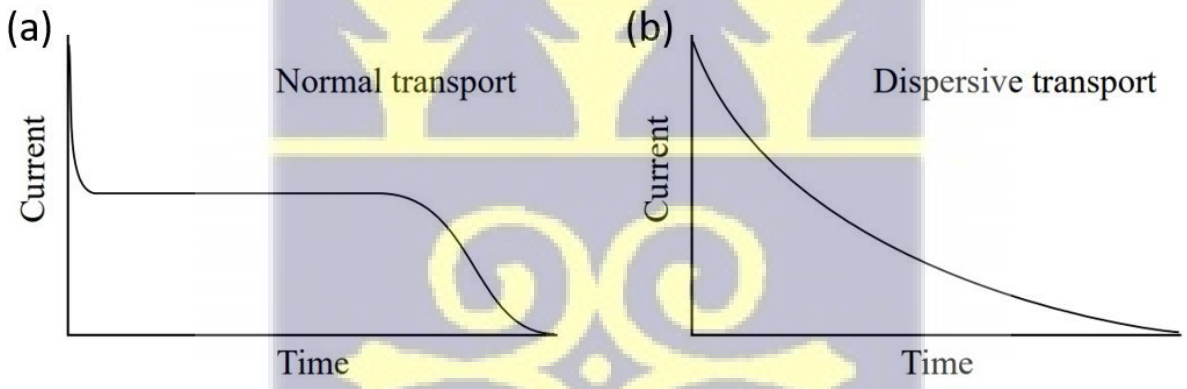

Figure 2.2: Current transients measured in time-of-flight experiments. (a) the plateau reveals the constant velocity of the carriers in normal transport. (b) the decay in the velocity of carriers in dispersive transport.

2.3 Factors affecting Charge Transport

Some factors that affect the charge transport in flexible PV are charge mobility, temperature, doping, crystal structure, and electric fields.

2.3.1 Charge mobility

Charge mobility refers to the ease with which charge carriers (electrons or holes) can move through a semiconducting material [43]. It is an important property of materials used in electronic devices, as it affects the conductivity of the material and the speed at which electronic devices can operate. The drift velocity of the charge carriers per unit electric field is used to define the charge mobility of a material which is measured in units of $cm^2V^{-1}s^{-1}$ [54], [55]. Materials with high charge mobility have fast-moving charge carriers that can easily respond to an applied electric field, while materials with low charge mobility have slow-moving charge carriers that are more resistant to movement.

2.3.2 Temperature

Temperature affects how charge carriers move within a substance. The number of charge carriers available for conduction rises as a function of temperature and the kinetic energy of the charge carriers. As a result, the material's conductivity may rise as the temperature rises [56]. However, at very high temperatures, phonon scattering can also become more pronounced, which reduces the mobility of the charges in the material [57].

2.3.3 Doping

In a PV cell, doping refers to the introduction of impurities into the semiconductor material that makes up the cell. These impurities, called dopants, can be either positive or negative and can affect the movement of charge carriers, such as electrons and holes, through the material [58]. Positively doped materials, also known as p-type materials, have an excess of holes and a deficiency of electrons. Negatively doped materials, also known as n-type materials, have an excess of electrons and a deficiency of holes [59].

Doping can affect the charge transport in a PV cell by changing the concentration of charge carriers and the way they move through the material. For example, in a p-type layer, the excess of holes can increase the charge transport of the material, making it easier for charge carriers to move through the cell. In an n-type PV cell, the excess of electrons increase the charge transport of the material [60].

Overall, doping can affect the efficiency of a PV cell [38] by changing the way that charge carriers move through the material. By carefully controlling the doping levels, it is possible to optimize the performance of the PV cell.

2.3.4 Crystal structure

The crystal structure of a material influences its charge carrier transport due to how ordered or disordered the structure is. Materials with a highly ordered and symmetric crystal structure have higher conductivity than those with a disordered or asymmetric crystal structure. For example, metals have a highly ordered crystal structure and thus exhibit high electrical conductivity, while amorphous or polycrystalline materials have a disordered or less symmetric structure; hence, exhibit lower conductivity [61]. Additionally, defects in the crystal can also affect charge transport by creating scattering centers for the charge which can impede their movement [62].

2.3.5 Electric fields

Charges move in the direction of the forces caused by the field when there is an electric field present [63]. The strength and the direction of the field, respectively, define the magnitude and the direction of the force exerted on the charge carriers. A substance with a high electrical conductivity will conduct electricity well because the charge carriers can move readily in response to the electric field [64]. However, in a material with a low electrical conductivity, the carriers may not be able

to move as easily thus, the material will have low electrical conductivity. Additionally, high electric fields can decrease the mobility of charge carriers, this effect is known as field-dependent mobility [65].

2.4 Characterization of Charge Transport

There are several methods that can be used to characterize charge transport in materials, including: Density Functional Theory (DFT), the continuity equation, Non-equilibrium Green's Function (NEGF), Boltzmann Transport Equation (BTE), and the Monte Carlo method. For this work, the continuity equation and DFT methods are the ones considered.

2.4.1 Density Functional Theory (DFT)

DFT sets out to provide a practical and efficient method for determining the electronic structure of a many-electron system [66] using their electron density, $n(\boldsymbol{r}) = \sum_i^{OCC} |\phi_i(\boldsymbol{r})|^2$. L. H. Thomas [67] and E. Fermi [68] proposed the first DFT for solids. Currently, Theorems by P. Hohenberg and W. Kohn are the solid theoretical foundations of modern DFT [69]. The central idea of DFT is to use the electron density as the basic variable, instead of the many-particle wave function, to describe the system developed by W. Kohn and L. Sham. The Kohn-Sham single-particle equation is as below:

$$\left(-\frac{1}{2}\nabla^2 + v_{xc}(\boldsymbol{r}) + v_h(\boldsymbol{r})\right)\phi_i(\boldsymbol{r}) = \epsilon_i \phi_i(\boldsymbol{r}) \qquad 2.1.1$$

Where v_h is the Hartree potential, which is defined as $\int d\boldsymbol{r}' \frac{n(\boldsymbol{r}')}{|\boldsymbol{r}-\boldsymbol{r}'|}$, ϵ_i is the single-particle energy [70], $\phi_i(\boldsymbol{r})$ is the wave function and $v_{xc}(\boldsymbol{r})$ is the exchange-correlation potential. Many local and non-local approximations to v_{xc} have been proposed in literature because the exact exchange-correlation potential[70] is unknown [71].

The Kohn-Sham equation is solved self-consistently because the operator in equation 2.1.1 depends on the electron density. The single-particle wave functions can be utilized to build the ground state density, which is used to compute the state parameters of interacting electrons such the total energy. In this work, local [72] and semi-local functional approximations are used for the exchange-correlation potential. Furthermore, hybrid functionals, [73]–[75] have been introduced and are dependent on the orbitals which take into account the exact exchange self-energy.

$$\sum\nolimits_X (\boldsymbol{r}, \boldsymbol{r}') = -\sum_j^N \phi_j(\boldsymbol{r})\phi_j^*(\boldsymbol{r}')v(\boldsymbol{r}, \boldsymbol{r}') \qquad 2.1.2$$

The hybrid potential is expressed as follows in the generalized Kohn-Sham formalism:

$$v_{xc}(\boldsymbol{r}, \boldsymbol{r}') = \alpha \sum\nolimits_X (\boldsymbol{r}, \boldsymbol{r}') + (1-\alpha)v_x(\boldsymbol{r}) + v_c(\boldsymbol{r}) \qquad 2.1.3$$

where v_{xc} has been split into two exchange potential (v_x) and correlation potential (v_c) and α is a constant.

Some advantages of using DFT for characterization of charge transport are:

1. Its ability to accurately predict the electronic structure and band structure of materials, which are important factors in determining charge transport properties.
2. It can handle large systems and complex geometries, making it well suited for studying the transport properties of real materials.
3. It can also be used to study materials in different environments, such as under strain, making it a powerful tool for understanding the effects of different conditions on charge transport.

With all these advantages, one major draw-back that is associated with DFT with respect to this work, is its limited accuracy for strongly correlated systems. In systems with strong electronic correlations such as high temperature superconductors, transition metal complexes, and strongly correlated electron systems, DFT is based on the mean-field approximation and is unable to completely capture the effects of strong electron-electron interactions. In these cases, a more advanced method such as the Hubbard model [76] is required.

2.4.2 Hubbard Correction

The Hubbard perturbation is a method used in DFT to account for the electron-electron interactions in systems with strong electronic correlations. The method is based on the Hubbard model, which describes the electronic structure of a system using a set of localized orbitals also called Wannier functions [77] and an on-site Coulomb repulsion term [78].

The Hubbard perturbation is implemented by adding a term to the total Hamiltonian of the system, called the Hubbard U term [79], which represents the repulsion energy between two electrons in the same localized orbital. The Hubbard U term can be written as:

$$U = U_{eff} \sum_{i,m} n_{i,m,\uparrow}\, n_{i,m,\downarrow}, \qquad 2.1.4$$

where U_{eff} is the on-site Coulomb repulsion, $n_{i,m,\uparrow}$ and $n_{i,m,\downarrow}$ are the occupation numbers for the up and down spin electrons in the localized orbital i and m.

The Hubbard U term is usually treated as a perturbation to the Kohn-Sham equations, which are the equations that are solved to obtain the electronic structure of the system in DFT. The perturbation is applied to the Hamiltonian of the system, which is written as:

$$\hat{H}' = \hat{H} + \Delta\hat{H}, \quad 2.1.5$$

where $\hat{H}$ is the Kohn-Sham Hamiltonian and $\Delta\hat{H}$ is the Hubbard U term.

The Hubbard perturbation method allows to take into account the electronic correlation effects and to improve the description of the electronic structure for systems with strong electronic correlation, but it also increases the computational cost of the calculations.

2.4.3 The Continuity Equation

It is possible to describe charge transport in a material or device using the continuity equation. The conservation of charge in a system is described by the continuity equation, which is a fundamental equation in physics. It specifies that the net flow of charge into or out of a particular volume equals the rate of change of charge density in that volume [80]. Mathematically, it can be written as:

$$\frac{\partial n}{\partial t} + \nabla.(nV) = G - R, \quad 2.1.6$$

where n is the charge density, t is the time, V is the velocity of the charge carriers [81], G is the generation rate, and R is the recombination rate. The right-hand side of the equation denotes the net flow of charge into or out of the given volume, while the left-hand side denotes the rate of change of charge density in that volume.

The continuity equation can be used to study the diffusion of charge carriers, the generation of charge carriers by light absorption, and the recombination of charge carriers. In PV cells, the analysis of charge carrier transport in the various layers of the device can be done using the continuity equation. By solving the continuity equation, it is possible to obtain information about

the current-voltage characteristics of the device and the efficiency of the device under different operating conditions [80].

2.5 Theory

From a first-principle perspective, the electronic properties which characterizes the transport of charges in a device is modelled by theoretically generating the total charge density (n_i) of the HTL. This can be solved using the density functional theory approach. The Kohn-Sham method [72] utilizes the variational approach by using the electron-electron potential of the density functional to generate the minimum energy and its corresponding molecular orbitals. With the many-body equation expressed as:

$$\hat{H}\,\psi_i(r_i) = \epsilon_i(r_i)\psi_i(r_i) \qquad 2.1.7$$

$\hat{H}$ is the Hamiltonian operator, ψ_i is the Kohn-Sham (KS) orbital [82], ϵ_i is the (KS) orbital energy, r_i represents the distance between two electrons.

The Hamiltonian operator is written as:

$$\hat{H} = T_{KS} + V_{ext} + V_H + V_{XC} \qquad 2.1.8$$

T_{KS} is the kinetic energy of particles in the KS orbitals, V_{ext} is an external potential of non-interacting electrons, V_H is the Hartree potential due to electrostatic interactions, and V_{XC} is the exchange correlation potential which includes all the remaining unknown terms. The kinetic energy is given explicitly as a function of the orbitals; however, it must be a unique functional of the charge density when the Hohenberg-Kohn arguments are applied. The kinetic energy is expressed as:

$$T_{KS}[n_i] = -\frac{\hbar^2}{2m}\sum_i \int \psi_i^* \nabla^2 \psi_i dr_i, \quad 2.1.9$$

the expression for the Hartree potential is also obtained as:

$$V_H[n_i] = e^2 \int \frac{n_i}{|r_i - r_i'|} dr_i' \quad 2.2.0$$

and the ground state energy becomes:

$$\epsilon_i = T_{KS} + \int (V_{ext} + V_H + V_{XC})\ dr_i \quad 2.2.1$$

We can finally write the Kohn-Sham equation as:

$$\left(-\frac{\hbar^2}{2m}\nabla^2 + V_{ext} + V_H + V_{XC}\right)\psi_i(r_i) = \epsilon_i \psi_i(r_i) \quad 2.2.2$$

A delocalized basis set is used to perform the calculation; hence, a plane wave basis is selected. The expression for the wave function with wave vector k is:

$$\psi_i = e^{ikr_i} \quad 2.2.3$$

where the sum of the expectation value of the KS orbitals gives the total electron density of the crystal

$$n_i = \sum_i \psi_i^* \psi_i = \sum_i |\psi_i|^2 \quad 2.2.4$$

Electrons are Fermions which obey the Pauli's exclusion principle. The Fermi-Dirac distribution statistics will be the best way to describe the arrangement of electrons in the energy levels. According to the Fermi-Dirac statistics, at temperature T, the concentration of electrons n_o at the bottom of the conduction band [7] is given as:

$$n_o = N_c f(E_c) \tag{2.2.5}$$

where N_C is the density of states in the conduction band and $f(E_c)$ is the Fermi-Dirac distribution function which describes the distribution of electrons in the conduction band. The distribution function can be represented with high precision as:

$$f(E_c) = \frac{1}{\exp\left(\frac{E_c - E_F}{k_B T}\right) + 1} \approx \exp\left(-\frac{E_c - E_F}{k_B T}\right) \tag{2.2.6}$$

Therefore, the electron density in the conduction band is written as:

$$n_o = N_c \exp\left(-\frac{E_c - E_F}{k_B T}\right) \tag{2.2.7}$$

For the valence band, the deficiency of electrons from the saturated situation gives rise to mobile carriers called holes. Similarly, the hole density is given as:

$$p_o = N_v[1 - f(E_v)] \approx N_v \exp\left(-\frac{E_v - E_F}{k_B T}\right) \tag{2.2.8}$$

N_V is the density of states in the valence band, and $f(E_v)$ is the distribution function in the valence band. It is crucial to note that the product, $n_o p_o$, is independent of the Fermi level, therefore, combining equations 2.2.7 and 2.2.8 we obtain:

$$n_o p_o = N_c N_v \, exp\left(-\frac{E_g}{k_B T}\right) \quad 2.2.9$$

For a material even with impurities, the total charge density is:

$$n_i^2 = n_o p_o \quad 2.3.0$$

The total charge density can be expressed as:

$$n_i = (N_C N_V)^{\frac{1}{2}} \, exp\left(-\frac{E_g}{2k_B T}\right) \quad 2.3.1$$

E_g is the energy band gap of the semiconductor, and k_B is Boltzmann's constant.

The local dynamical diffusion current density within a lattice is expressed in one dimension represented by x to reduce complexity and computational cost [83], [84]. In the presence of an electric field $E(x)$, the carrier density gradient $\frac{dn(x)}{dx}$ associated with the drift contribution, J_d has a diffusion contribution, J_D [84].

This diffusion contribution can be expressed as:

$$J_D = -qD\frac{dn(x)}{dx} \quad 2.3.2$$

Also, the drift contribution is written as:

$$J_d = |q|n(x)\mu(x)E(x) \quad 2.3.3$$

Furthermore, the expression for the diffusion coefficient is given as:

$$D = \frac{\mu(x) k_B T}{q} \qquad 2.3.4$$

Where μ is the carrier mobility. If D_e and D_p represent the diffusion coefficients for electrons and holes respectively, and $p(x)$ represents the hole density, then the electron diffusion current densities, J_e can be represented as:

$$J_e(x) = qD_e \frac{dn(x)}{dx} \qquad 2.3.5$$

and the hole diffusion current densities J_p, can also be written as:

$$J_p(x) = -qD_p \frac{dp(x)}{dx} \qquad 2.3.6$$

For an intrinsic material, the sum of J_e and J_p will give us the local dynamic diffusion current, J_{diff}.

$$J_{diff} = k_B T \left(\mu_e(x) - \mu_p(x)\right) \frac{dn(x)}{dx}, \qquad 2.3.7$$

μ_p and μ_e are mobilities for holes and electrons respectively. The ohmic current (J_σ) is also described as:

$$J_\sigma = qn(x)\left(\mu_e(x) + \mu_p(x)\right)E(x) \qquad 2.3.8$$

The sum of the local dynamic diffusion and ohmic current densities give the total current density [85], J_{total}:

$$J_{total} = k_B T\left(\mu_e(x) - \mu_p(x)\right)\frac{dn(x)}{dx} + qn(x)\left(\mu_e(x) + \mu_p(x)\right)E(x) \quad 2.3.9$$

In an open circuit configuration, the semiconductor has no current flowing across it, therefore J_{total} is zero. This means that J_{diff} must be equal and opposite to J_{σ}.

$$J_{\sigma} = -J_{diff} \quad 2.4.0$$

This is written in full as:

$$qn(x)\left(\mu_e(x) + \mu_p(x)\right)E(x) = -k_B T\left(\mu_e(x) - \mu_p(x)\right)\frac{dn(x)}{dx} \quad 2.4.1$$

Now we can have an expression for the electric field as:

$$E(x) = \frac{-k_B T}{q}\left(\frac{\mu_e(x) - \mu_p(x)}{\mu_e(x) + \mu_p(x)}\right)\frac{1}{n(x)}\frac{dn(x)}{dx} \quad 2.4.1$$

A potential difference is created between two points in a semiconductor by the electric field. Assuming x_1 and x_2 positions, the potential difference (V) between them will be:

$$V = -\int_{x_1}^{x_2} E(x)dx, \quad 2.4.2$$

further expressed as:

$$V_{OC} = \int_{x_1}^{x_2} \frac{k_B T}{q} \left(\frac{\mu_e(x) - \mu_p(x)}{\mu_e(x) + \mu_p(x)} \right) \frac{1}{n(x)} \frac{dn(x)}{dx} dx \qquad 2.4.3$$

Equation 2.4.3 represents the open circuit voltage between two points [84].

CHAPTER 3

In this section, the methods and procedures used to characterize the hole transport layer are discussed. It involves a first-principles study and a device performance simulation. The hole transport layer materials chosen for this work are nickel oxide (NiO) and copper doped nickel oxide (Cu:NiO). These materials were chosen for this work due to their high hole mobility, stability and compatibility with a wide range of semiconductors.

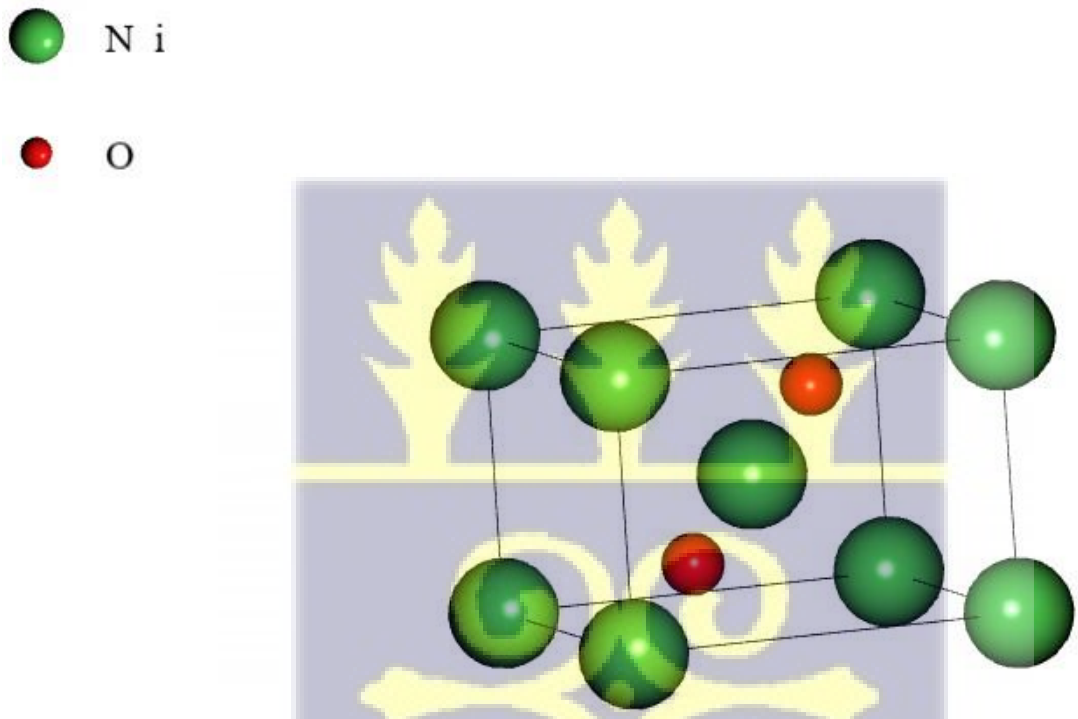

Figure 3.1: Crystal structure of NiO

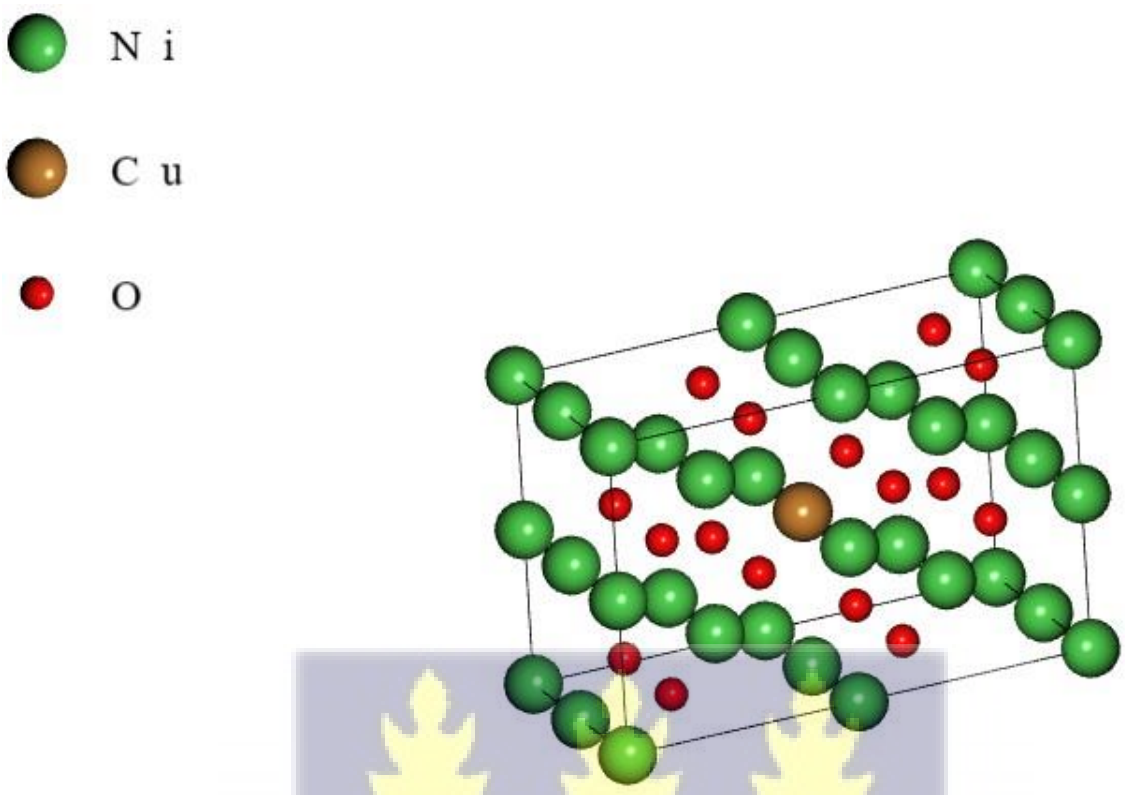

Figure 3.2: Crystal structure of Cu:NiO

3.1 First-principles study

First-principles calculations were performed on NiO and Cu:NiO using density functional theory as implemented in the Quantum Espresso software package [86], [87]. To begin, the crystal structures of the materials are stable to obtain the minimum energy of the system at low pressure (under 1kPa). The system's ground state electron density and energy are then calculated using self-consistent and non-self-consistent fields. In the end, both materials' band structures and density of states are computed.

3.1.1 Relaxation

Relaxation of a crystal structure refers to the process of finding the lowest energy configuration of a system by allowing the atoms to move from their initial positions. This is done by using a numerical optimization algorithm, such as conjugate gradient or steepest descent, to minimize the

total energy of the system. The algorithm iteratively adjusts the positions of the atoms until a convergence criterion is met, such as a specified threshold for the change in energy or the forces on the atoms. During this process, the electronic structure of the system is recalculated at each step using the updated atomic positions.

3.1.2 Self-Consistent Field (SCF) Calculation

After relaxing the crystal system, a self-consistent field calculation is conducted. Finding the system's ground-state electron density and energy is the aim of a SCF calculation. An initial estimation of the electron density serves as the basis for the SCF calculation. Then the electronic potential, $V(r)$, is calculated from the electron density using the following equation:

$$V(r) = V_{ext}(r) + V_H(r) + V_{XC}(r) \qquad 3.1.1$$

where $V_{ext}(r)$ is the external potential, $V_H(r)$ is the Hartree potential, and $V_{XC}(r)$ is the exchange-correlation potential. Once the potential is calculated, the electron wavefunctions and energies are determined by solving the Kohn-Sham equation (2.2.2). The electron density is then updated by summing over the occupied wavefunctions. The process is then repeated, using the updated electron density to calculate a new potential, and so on, until the electron density and potential have converged to a self-consistent solution. The final solution of the SCF calculation gives the ground-state electron density and energy of the system.

3.1.3 Hubbard Correction

This method involves adding an on-site Coulomb repulsion term, U, to the standard DFT Hamiltonian [88] in order to account for the strong electron-electron interactions between the p-orbitals of O and the d-orbitals of Ni [43]. The Hubbard U parameter is calculated using the linear response approach. This method involves calculating the change in the total energy of the system as a small perturbation is applied [89] to the electron density. The perturbation can be introduced

by adding or removing an electron from a localized atomic or molecular orbital, or by adjusting the occupation of an existing electron. By fitting the calculated energy change to a linear function, the Hubbard U parameter can be extracted. The Hubbard U parameter was calculated to be 7.6eV.

3.1.3 Non-Self-Consistent Field (NSCF) Calculation

In this case, the potential is fixed to the potential of the ground state electron density, and the wave functions and energies are calculated along a path in k-space (i.e. the reciprocal space of the crystal lattice) [90]. The equation for the calculation of electronic wave functions and energies in a non-self-consistent field calculation is the time-independent Schrödinger equation, which is given in equation (2.1.7).

3.1.4 Bands Structure

To calculate the band structure, a series of calculations for different wavevectors k along high-symmetry lines in the Brillouin zone is performed. At each k-point, the Kohn-Sham equation is solved to determine the electronic wavefunctions and energies. The energies are then plotted as a function of k-path to produce the band structure.

3.1.5 Density of States (DOS)

In DFT, the DOS is calculated by taking the derivative of the integrated electron density with respect to energy [91]. The integrated electron density, also known as the electron density of states (EDOS), is given by:

$$EDOS(E) = \frac{2}{N} \int d^{3k}\, \Theta(E - E_k), \qquad 3.1.2$$

where N is the number of electrons, k is the wave vector, E_k is the energy of the kth state, and Θ is the Heaviside step function. The DOS is then calculated by taking the derivative of the EDOS with respect to energy:

$$DOS(E) = \frac{dEDOS(E)}{dE} \qquad 3.1.2$$

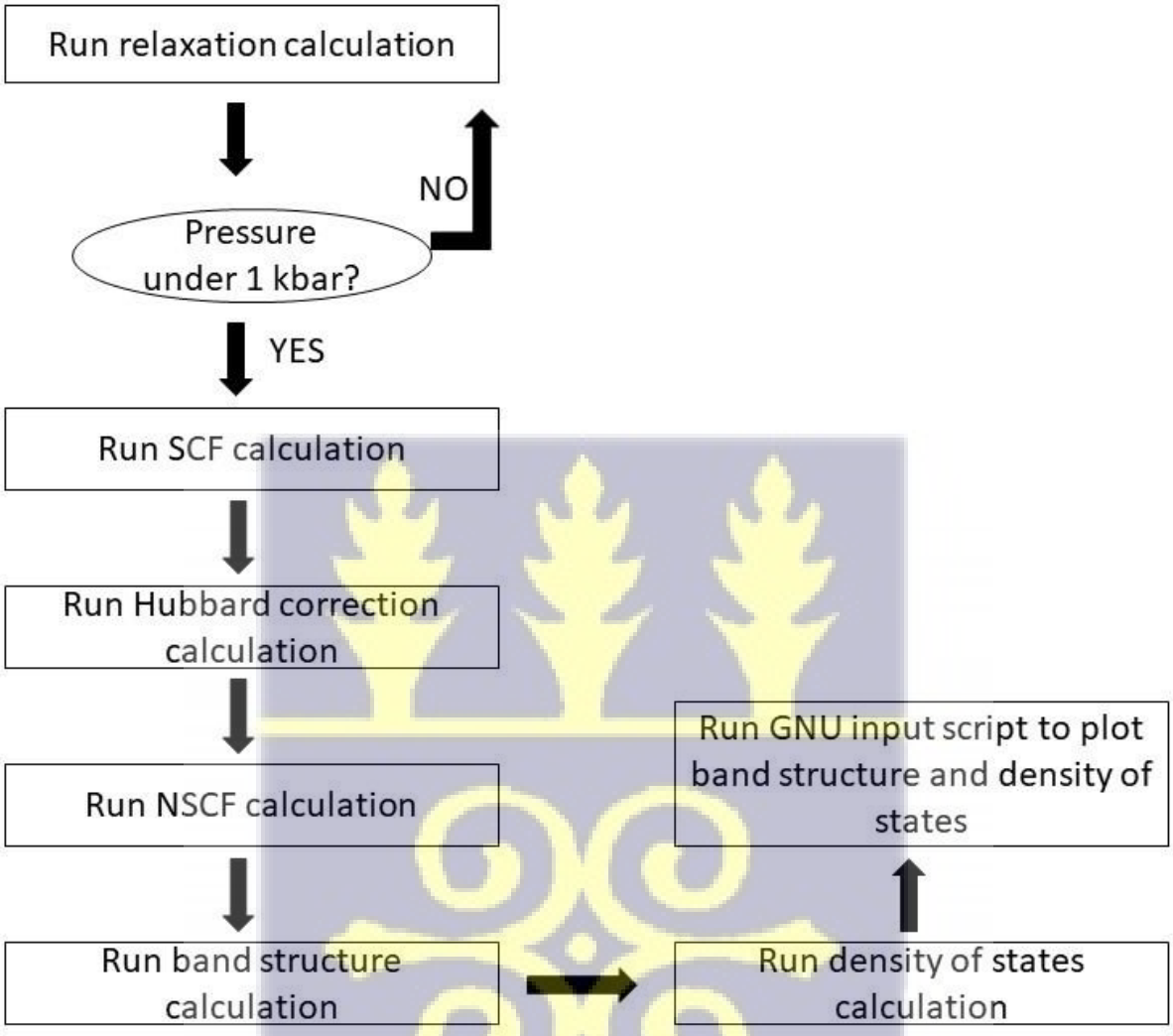

Figure 3.3: Flowchart of the methodology used in first-principles computation.

3.2 Device Performance Simulation

A Solar cell Capacitance Simulator (SCAPS) software package [92] is used to investigate the performance of the PV device. The Poisson's equation, the carrier continuity equation (2.1.6), and the charge carrier drift diffusion equations (2.3.5 and 2.3.6) are the foundations of the simulation

software. The performance of the PV device was simulated with different composite HTLs against two different active layers. The first simulation employed a fullerene (P3HT/PCBM) blend as an active layer and the second used a perovskite ($CH_3NH_3PbI_3$) as an active layer. The device configurations for the simulations are shown in Figure 3.4.

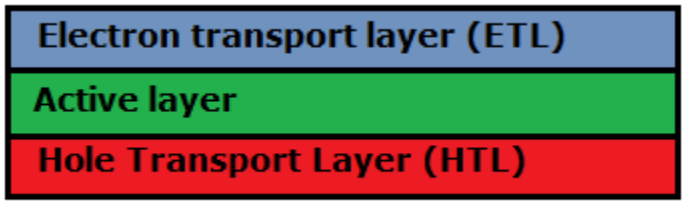

Figure 3.4: Schematic configuration of device layers.

The thickness data in SCAPS is used to define the physical dimensions of the various layers within a solar cell structure. These dimensions, in turn, influence the optical and electrical behaviour of the solar cell, making thickness a critical parameter for simulating and optimizing solar cell performance. Thicknesses are fine-tuned to achieve desired performance outcomes and better understand the behaviour of solar cells. The band gap, electron affinity, dielectric permittivity, conduction band density of states, valence band density of states, electron mobility, hole mobility, shallow donor density and shallow acceptor density are fundamental properties that describe the electronic characteristics of each semiconductor layer in the PV cell. SCAPS uses these parameter to calculate the optical and electrical characteristics of the PV cell to be simulated. Table 3.1 lists the parameters and the associated values for the simulations.

Table 3.1. I-V characteristic simulation parameters.

PARAMETERS	P3HT:PCBM [93]	PEDOT:PSS [94]	NiO [95]	Cu:NiO	$CH_3NH_3PbI_3$ [96]
Thickness (nm)	90	100	125	125	245
Band gap (eV)	1.05	1.60	3.04	1.65/2.63	1.55
Electron affinity (eV)	3.95	3.40	4.50	2.10	3.90
Dielectric permittivity	3.5	3.0	9.4	11.7	6.5
CB density of states (cm^{-3})	$1.00x10^{19}$	$2.20x10^{15}$	$4.00x10^{19}$	$3.78x10^{16}$	$1.80x10^{18}$
VB density of states (cm^{-3})	$1.00x10^{19}$	$1.80x10^{18}$	$1.00x10^{18}$	$3.78x10^{16}$	$1.80x10^{19}$
Electron mobility ($cm^2V^{-1}s^{-1}$)	10^{-3}	10	10.50	5.58	0.5
Hole mobility ($cm^2V^{-1}s^{-1}$)	10^{-3}	10^{-3}	25.0	30.0	0.5
Shallow donor density (cm^{-3})	10^{18}	$3.17x10^{14}$	$1x10^{21}$		
Shallow acceptor density (cm^{-3})				$3x10^{18}$	$1x10^{19}$

CHAPTER 4

4.1 Results and Discussion

The band structure, density of states and I-V characteristics of pristine NiO and Cu:NiO were analyzed in this chapter. NiO has an FCC crystal structure with a lattice constant of $a = 4.315$ Å [82] and possesses a type-II antiferromagnetic spin coupling along the [111] direction and thus requires a rhombohedral primitive unit cell [97] which consists of 4 atoms (2 Ni atoms and 2 O atoms). To examine the effects of doping NiO with a Cu atom, a supercell containing 15 Ni atoms, 16 O atoms and 1 Cu atom was used which accounts for ~6% doping. Two scenarios of the doped material were examined. The first scenario involves the relaxation of the supercell structure before the first-principle calculations whilst the second scenario did not go through relaxation before the first-principle calculation. The band structures and density of states of the primitive cell and both stable and unstable supercell structures are presented.

4.2 Band structure

The band structure of NiO yields an indirect band gap with the conduction band (CB) minimum located at the Γ point and the valence band (VB) maximum located at the Z point. NiO is known as an antiferromagnetic semiconductor with an indirect band gap. In its pure form, the electronic structure of NiO is characterized by a partially filled d-orbital, leading to antiferromagnetic ordering. Hybridization of Ni's d-orbitals with the oxygen p-orbitals results in the formation of energy bands. This hybridization primarily involves d-d and p-d orbitals. The partial filling of Ni's d-band contributes to the semiconducting behavior and indirect band gap of NiO. The bands are separated as a result of the hybridization, and the band minimum and maximum are not located at the same k-path in the first Brillouin zone. The Fermi level was calculated to be 13.812eV with a band gap (E_g) of 3.04 eV as shown in Figure 4.1.

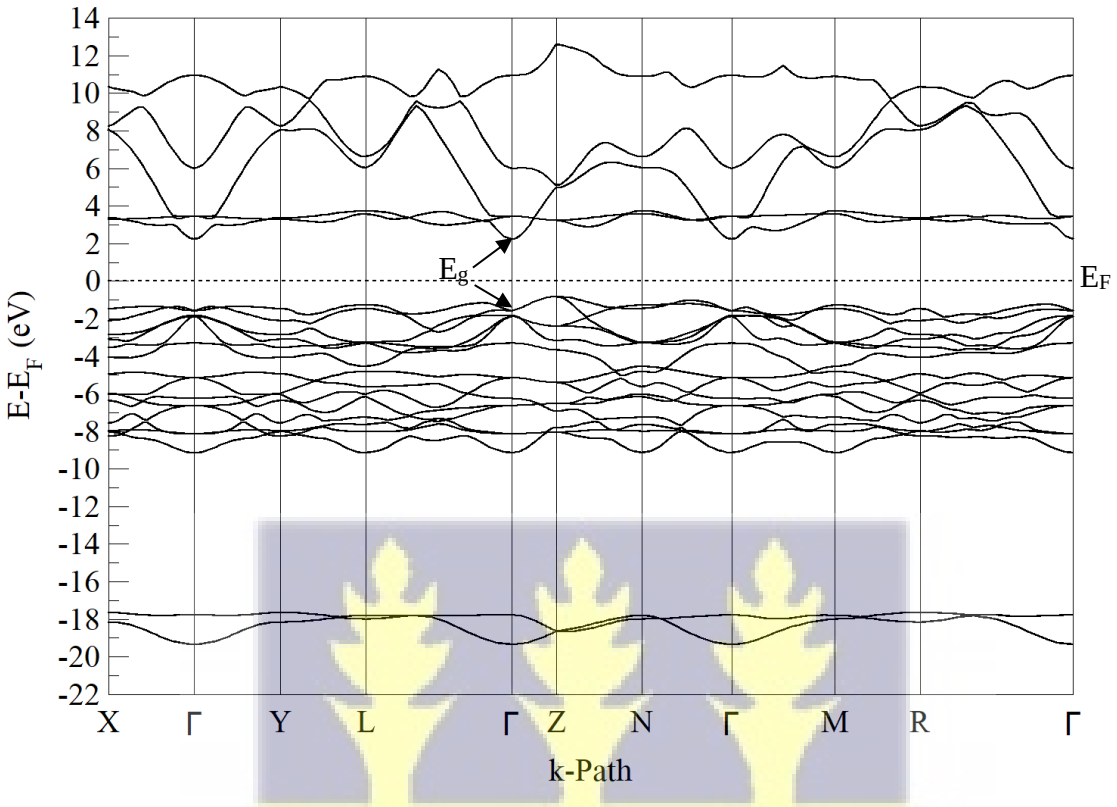

Figure. 4.1: Band structure of NiO. All energies are relative to the Fermi level E_F.

Cu ions have a single valence electron in the 3d orbital while Ni ions have valence electrons in the 3d and 4s orbitals, therefore, when the Cu ion is substituted for a Ni ion in the NiO crystal lattice, they introduce new energy levels into the band structure, resulting in additional bands for both stable and unstable supercell structures. Cu's d-orbitals hybridizes with the Ni and O orbitals in the host lattice. This hybridization alters the band structure by introducing new energy levels within the band gap, which results in the direct band gap observed in Figure 4.2.

For both structures of Cu:NiO (stable and unstable), the CB minimum and VB maximum occur at the Γ point which yields a direct band gap [98]. This is as a result of the creation of a hole in the valence band by the Cu ion. The hole acts as a carrier by adding states and allows for a direct transition from the valence band to the conduction band. The additional bands increase the carrier concentration of the crystal making it more conductive.

A look at the stable supercell structure reveals that, the lattice constants and the atomic positions are optimized to the ground state. The Fermi level is calculated to be 11.591 eV with a band gap of 1.65 eV.

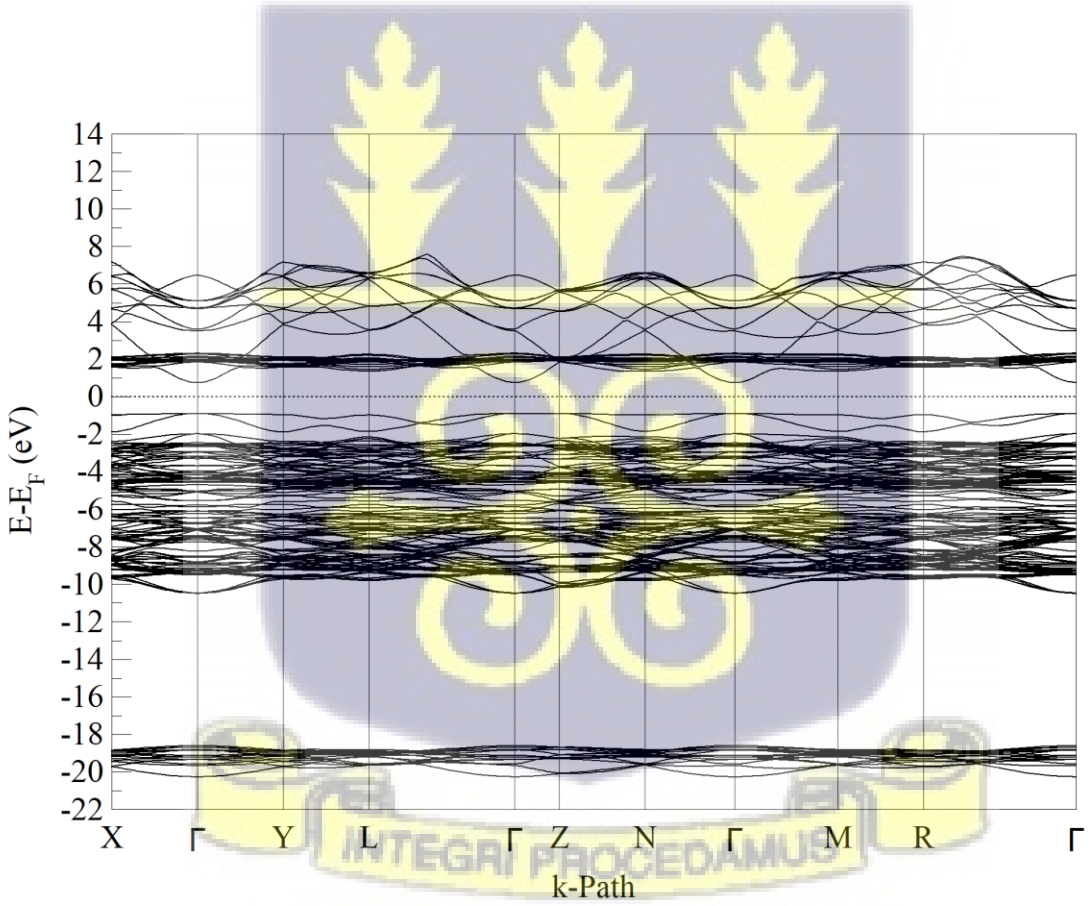

Figure 4.2: Band structure of Cu:NiO (stable).

On the other hand, the unstable supercell structure has its lattice constant and atomic positions kept fixed with any optimizations on the electronic structure hence, the crystal structure does not reflect the ground state energy [99]. The Fermi level is calculated to be 13.477eV with a band gap of 2.63 eV as shown in Figure 4.3.

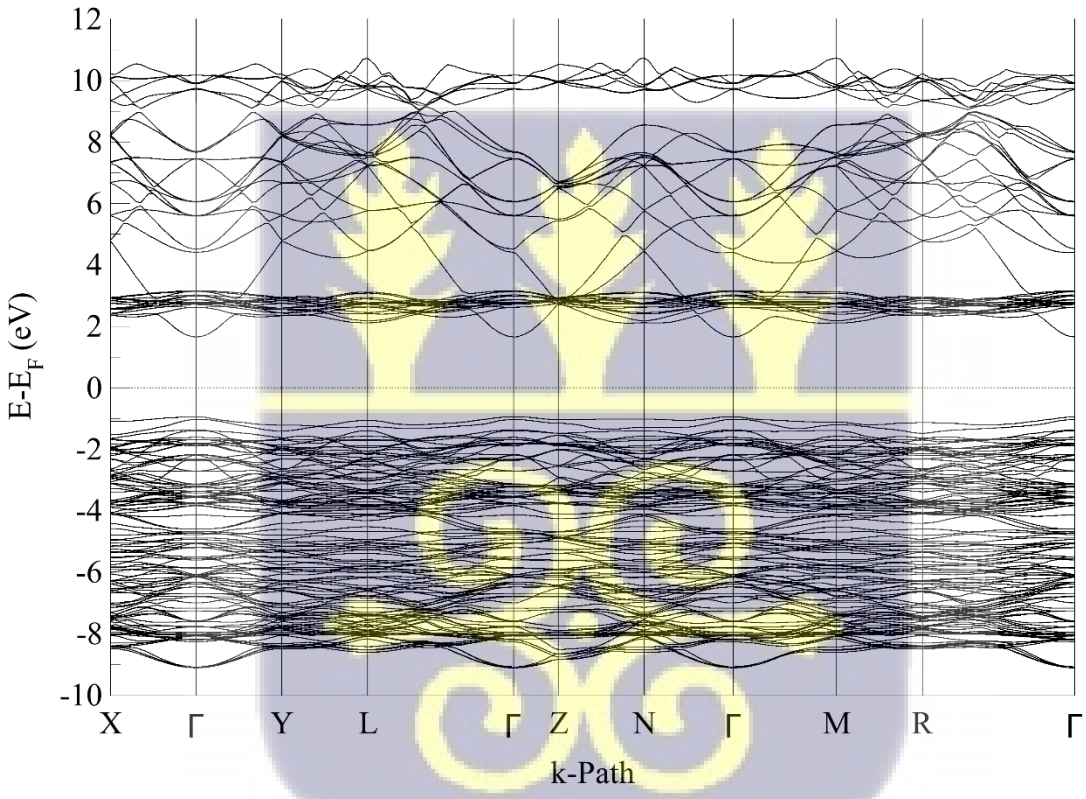

Figure 4.3: Band structure for Cu:NiO (unstable).

Table 4.1 shows the band gap and Fermi level calculated for NiO, Cu:NiO (stable) and Cu:NiO (unstable)

Table 4.1: Band gap and Fermi level for NiO, Cu:NiO (stable) and Cu:NiO (unstable)

Material	Band gap (eV)	Fermi level (eV)
NiO	3.04	13.812
Cu:NiO (stable)	1.65	11.591
Cu:NiO (unstable)	2.63	13.477

4.3 Density of States (DOS)

The p-type character of NiO is confirmed by the density of states for NiO, which is depicted in Figure 4.4. It shows that the Fermi level is closer to the valence band than to the conduction band. The Ni and O atoms in the crystal lattice bond with each other to produce the valence band [100]. Close to the Fermi level in the valence band, the 2p-orbital of O is dominant while in the conduction band, the 3d-orbital of Ni is dominant [101].

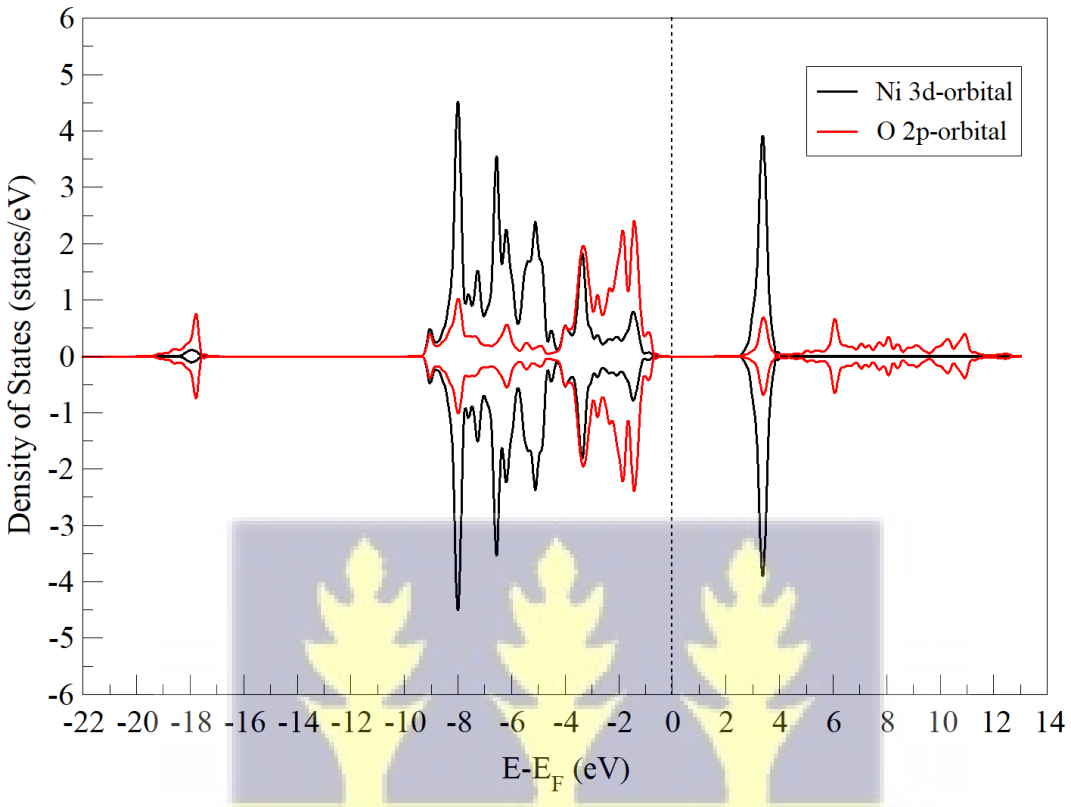

Figure 4.4: Density of states of NiO (spin up and spin down).

For Cu:NiO, the DOS for both stable and unstable crystal structure shows that there are inter-bands occurring between the 3d-orbital of nickel and the 3d-orbital of Cu close to the Fermi level. Because of the Cu ion's existence, the lattice symmetry is reduced, increasing the number of electron states that are possible. The defect created by the substitution of Cu ion for Ni ion has given rise to additional electronic states near the bandgap.

Due to the optimization of the lattice constant and the atomic positions in the stable structure, the additional band introduced by the Cu ion appears very close to the Fermi level. These optimized

new states are responsible for the narrowing of the band gap in the crystal structure which can be seen in Figure 4.5.

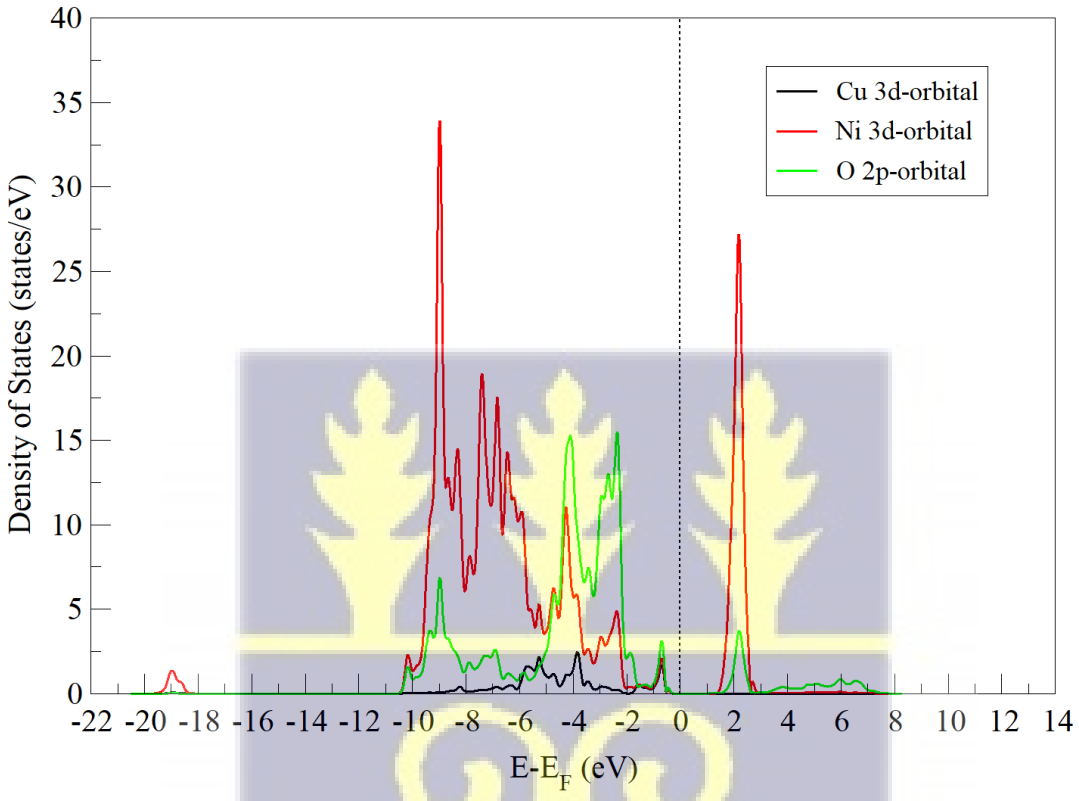

Figure 4.5: Density of states (spin up) for Cu:NiO (stable).

The unstable supercell structure had its lattice constant and atomic positions remain fixed therefore, the additional states introduced by the 3d-orbital of the Cu ion are relatively further from the Fermi level which results in a wide band gap of 2.63 eV as compared to the stable supercell structure (see Figure 4.6).

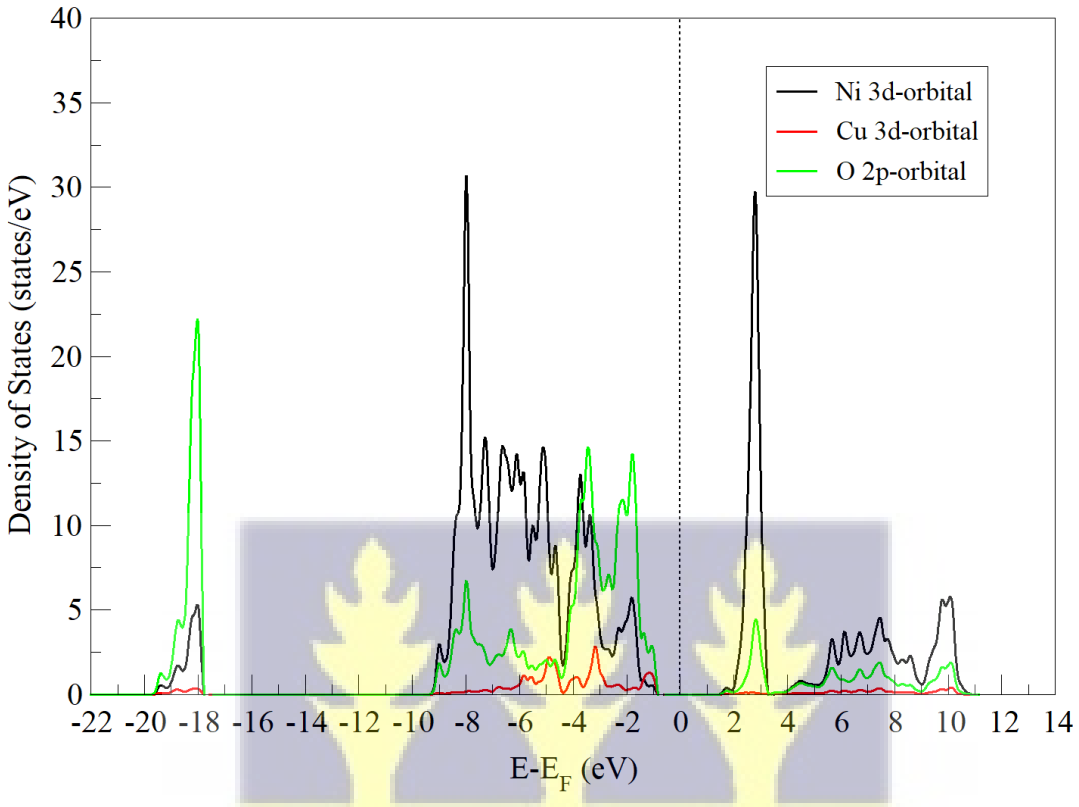

Figure 4.6: Density of states (spin up) for Cu:NiO (unstable).

4.4 Current-Voltage (I-V) characteristics

The performance of the PV device was simulated with different composite HTLs against two different active layers. The first simulation employed a fullerene (P3HT/PCBM) blend as an active layer and the second used a perovskite ($CH_3NH_3PbI_3$) as an active layer. The HTLs simulated were PEDOT:PSS , PEDOT:PSS/NiO, PEDOT:PSS/Cu:NiO (stable) and PEDOT:PSS/Cu:NiO (unstable) composite.

For the P3HT/PCBM blend as shown in Figure 4.7, PEDOT:PSS recorded a short-circuit current density of 13.863 $mAcm^{-2}$ whilst PEDOT:PSS/NiO, PEDOT:PSS/Cu:NiO (stable) and PEDOT:PSS/Cu:NiO (unstable) recorded 12.264 $mAcm^{-2}$ and 12.532 $mAcm^{-2}$ 11.995 $mAcm^{-2}$ respectively. The open-circuit voltage for PEDOT:PSS, PEDOT:PSS/NiO, PEDOT:PSS/Cu:NiO (stable) and PEDOT:PSS/Cu:NiO (unstable) are 0.835 V, 0.990 V, 1.020 V and 1.047 V respectively.

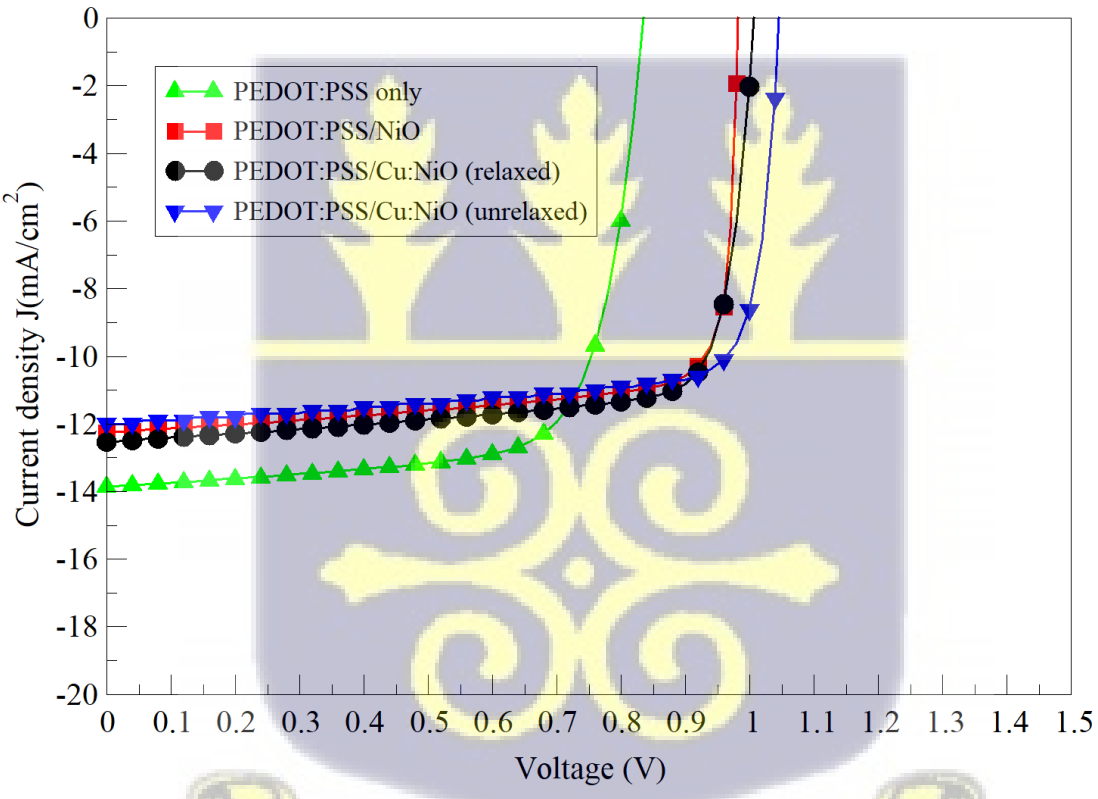

Figure 4.7: I-V characteristics of different composite HTLs with a fullerene blend active layer.

Figure 4.8 shows the I-V graph for the perovskite used as an active layer. The short-circuit current densities for PEDOT:PSS, PEDOT:PSS/NiO, PEDOT:PSS/Cu:NiO (stable) and PEDOT:PSS/Cu:NiO (unstable) are 11.692 $mAcm^{-2}$, 12.884 $mAcm^{-2}$, 15.693 $mAcm^{-2}$ and 17.447 $mAcm^{-2}$ respectively. Their corresponding open- circuit voltages are 1.230 V, 1.296 V, 1.316 V and 1.431 V respectively.

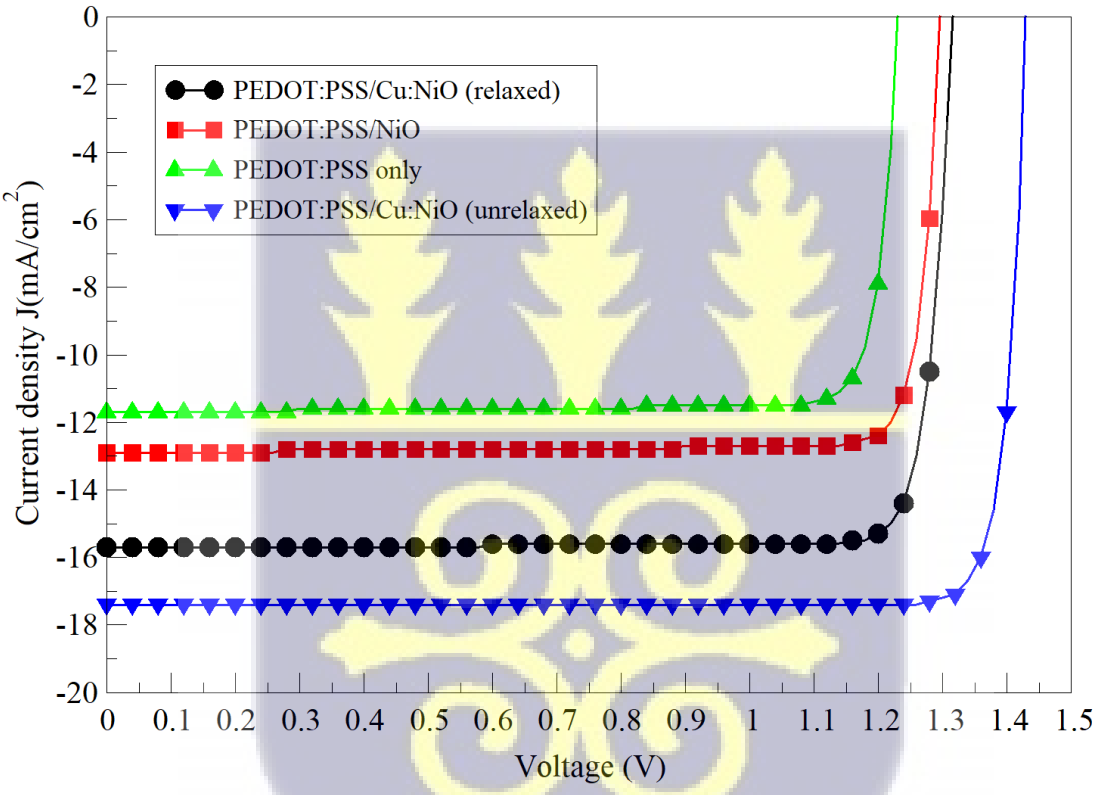

Figure 4.8: I-V characteristics of different composite HTLs with a perovskite active layer.

The efficiencies of the composite HTLs in different device configurations are displayed in Table 4.2 and Table 4.3.

Table 4.2. I-V characteristics and performance efficiency obtained for fullerene blend.

HTL[102]	**Jsc(mAcm^{-2})**	$V_{OC}(V)$	**FF(%)**	**PCE(%)**
PEDOT:PSS only	13.863	0.835	72.34	8.38
PEDOT:PSS/NiO	12.264	0.990	77.34	9.54
PEDOT:PSS/Cu:NiO (stable)	12.532	1.020	77.21	9.75
PEDOT:PSS/Cu:NiO (unstable)	11.995	1.047	77.93	9.79

Table 4.3. I-V characteristics and performance efficiency obtained for perovskite.

HTL[102]	**Jsc(mAcm^{-2})**	$V_{OC}(V)$	**FF(%)**	**PCE(%)**
PEDOT:PSS only	11.692	1.230	87.99	12.66
PEDOT:PSS/NiO	12.884	1.296	88.78	14.83
PEDOT:PSS/Cu:NiO (stable)	15.693	1.316	88.91	18.37
PEDOT:PSS/Cu:NiO (unstable)	17.447	1.431	90.27	22.53

The efficiencies obtained from combining the various composite HTLs with fullerene blend are: 8.38%, 9.54%, 9.75% and 9.79% for PEDOT:PSS, PEDOT:PSS/NiO PEDOT:PSS/Cu:NiO (stable) and PEDOT:PSS/Cu:NiO [103] (unstable) respectively. The perovskite device efficiencies are: 12.66%, 14.83% 18.37%, and 22.53% for PEDOT:PSS, PEDOT:PSS/NiO, PEDOT:PSS/Cu:NiO (stable) and PEDOT:PSS/Cu:NiO (unstable) respectively.

CHAPTER 5

5.1 Conclusion

On pristine NiO and Cu:NiO, first principle calculations were carried out utilizing density functional theory as applied in the Quantum Espresso software. Two instances of the doped supercell structure (Cu:NiO) were analyzed. The first instance involved a stable structure of Cu:NiO whilst the second instance involved an unstable structure of Cu:NiO.

As a result of the strong electron-electron interactions between the 2p-orbitals of O and the 3d-orbitals of Ni, a Hubbard correction term known as "Hubbard U" term was required to add an on-site Coulomb term to the total Hamiltonian of the structure. The "Hubbard U" term was calculated to be 7.6 eV.

Pristine NiO showed a band gap of 3.04 eV and the Fermi level was calculated to be 13.812 eV. The hybridization of the 2p-orbitals of O and the 3d-orbitals of Ni revealed the band structure of NiO to have an indirect band gap with the CB minimum located at the point and the VB maximum located at the Z point.

Both stable and unstable supercell structures of Cu:NiO showed a direct band gap with the CB minimum and the VB maximum occurring at the Γ point. This occurred due to the Cu ion's production of a hole in the valence band, which adds new states and enables a direct passage of electrons from the valence band to the conduction band. The extra bands boost the crystal's carrier concentration, making it more conductive. The stable supercell structure had its lattice constant and atomic positions optimized to the ground state hence its band gap was obtained to be 1.65 eV and the Fermi level was calculated to 11.591 eV. The optimization of the electronic structure led to the new states introduced by the Cu ion into the structure appearing close to the Fermi level accounting for the narrow band gap observed.

The unstable structure did not have any optimization calculations performed on its lattice constant and the positions of the atoms. This resulted in the new states introduced by the Cu ion appearing further from the Fermi level relative to the one observed in the stable structure hence, a wide band was achieved. The band gap obtained for the unstable structure was 2.63 eV and the Fermi level was calculated to be 13.477 eV.

This suggested that Cu:NiO (unstable) will perform well as a HTL as compared to NiO and Cu:NiO (stable) due to its wide direct band gap nature and extra states in the valence to aid in the conduction of holes.

I-V delineation was performed using two different active layers (i.e., fullerene blend and perovskite). Three different composite HTLs were simulated with the two active layers mentioned. These HTLs included: PEDOT:PSS, PEDOT:PSS/NiO, PEDOT:PSS/Cu:NiO (stable) and PEDOT:PSS/Cu:NiO (unstable).

For the fullerene blend, Cu:NiO (unstable) composite showed the highest efficiency with a PCE of 9.79% as predicted from the solar cell simulation, with an open-circuit voltage of 1.041 V and a shot-circuit current of 11.995 $mAcm^{-2}$.

The PV device with the perovskite active layer showed more promising results. Again, the prediction of the solar cell simulation showed that Cu:NiO (unstable) achieved the highest efficiency with a PCE of 22.53%. The open-circuit voltage recorded was 1.431 V and the short-circuit current was 17.447 $mAcm^{-2}$.

5.2 Recommendations

Some recommendations for future works include, device simulations incorporating temperature-dependent material properties and taking into account temperature-induced changes in the device

structure can help to predict the temperature dependence of charge transport. The simulation can shed light on the relationship between charge transport and temperature, especially how temperature affects the electrical conductivity of the material. The results of the simulation can be used to optimize the performance of PV devices for different operating temperatures. The simulations can also be used to evaluate the reliability and long-term performance of devices under varying temperature conditions.

Also, humidity-dependent charge transport characterization can also be performed to ascertain the charge transport behavior of a PV device under different humidity conditions. The simulation will include how humidity affects the device's electronic characteristics, such as its electrical conductivity and the mobility of its charge carriers, as well as how moisture affects the device's structural alterations. This can be used to predict the lifespan of the device and how the performance of the device will change over the period of its lifespan.

The performance of a PV cell is influenced by the concentration of impurities, or "dopants," added to the charge transport layers. The doping percentage refers to the concentration of these impurities. Another aspect that can be explored in future works will be to take into consideration how different doping percentages of the HTL affects the performance of the PV device. This will help in finding the optimal doping percentage for a charge transport layer which requires a balance between increased conductivity and the maintenance of a high open-circuit voltage [104].

REFERENCES

[1] A. Goetzberger, C. Hebling, and H.-W. Schock, "Photovoltaic materials, history, status, and outlook," *Reports A Rev. J.*, pp. 1–46, 2002, doi: 10.1016/0927-0248(92)90015-H.

[2] D. Castano, "Physics Overview of Solar Energy," in *Natural and Artificial Photosynthesis: Solar Power as an Energy Source*, 2013, pp. 1–12.

[3] K. M. Manoj, "Oxygenic photosynthesis : Critiquing the standing explanations and proposing explorative solutions based in murburn concept," *Open Sci. Framew.*, 2019.

[4] M. A. Green, "Photovoltaics: Coming of age," *Conf. Rec. IEEE Photovolt. Spec. Conf.*, vol. 1, pp. 1–8, 1990, doi: 10.1109/pvsc.1990.111582.

[5] W. G. Adams and R. E. Day, "The Action of Light on Selenium," *Proc. R. Soc.*, vol. A25, p. 113, 1877.

[6] A. Einstein, "On a Heuristic Point of View Concerning the Production and Transformation of Light," 1905, doi: 10.2307/j.ctvkwnmwf.18.

[7] C. J. Chen, *Physics of Solar Energy*. New York: John Wiley & Sons, Inc., Hoboken, New Jersey, 2011.

[8] L. Szabó, "The History of Using Solar Energy," in *2017 International Conference on Modern Power Systems (MPS)*, 2017, no. 21.

[9] L. L. Kazmerski, "The Bell Telephone Laboratories Discovery : Ushering in Our Modern Age of Solar Photovoltaics," in *Photovoltaics for Sustainable Electricity and Buildings*, 2017, pp. 15–23.

[10] M. A. B. Gapol, M. P. Balanay, and D. H. Kim, "Molecular engineering of

tetraphenylbenzidine-based hole transport material for perovskite solar cell," *J. Phys. Chem. A*, vol. 121, no. 6, pp. 1371–1380, 2017.

[11] NREL, "Best Research-Cell Efficiencies," p. 2020, 2020.

[12] B. Pratap, S. Kumar, and P. Kumar, "Materials Today : Proceedings Solar PV cell materials and technologies : Analyzing the recent developments," *Mater. Today Proc.*, vol. 43, pp. 2843–2849, 2021, doi: 10.1016/j.matpr.2021.01.003.

[13] A. Khatibi, F. Razi Astaraei, and M. H. Ahmadi, "Generation and combination of the solar cells: A current model review," *Energy Sci. Eng.*, vol. 7, no. 2, pp. 305–322, 2019, doi: 10.1002/ese3.292.

[14] K. D. G. I. Jayawardena, L. J. Rozanski, C. A. Mills, M. J. Beliatis, N. A. Nismy, and S. R. P. Silva, "'Inorganics-in-Organics': recent developments and outlook for 4G polymer solar cells," *Nanoscale*, vol. 5, pp. 8411–8427, 2013, doi: 10.1039/c3nr02733c.

[15] D. D. B. Mesquita, J. L. D. S. Silva, H. S. Moreira, M. Kitayama, and M. G. Villalva, "A review and analysis of technologies applied in PV modules," *2019 IEEE PES Conf. Innov. Smart Grid Technol. ISGT Lat. Am. 2019*, 2019, doi: 10.1109/ISGT-LA.2019.8895369.

[16] J. Friedrich, W. von Ammon, and G. Müller, *Czochralski Growth of Silicon Crystals*, Second Edi., vol. 2. Elsevier B.V., 2015.

[17] J. E. Cotter, J. H. Guo, P. J. Cousins, M. D. Abbott, F. W. Chen, and K. C. Fisher, "P-type versus n-type silicon wafers: Prospects for high-efficiency commercial silicon solar cells," *IEEE Trans. Electron Devices*, vol. 53, no. 8, pp. 1893–1901, 2006, doi: 10.1109/TED.2006.878026.

[18] M. A. Green *et al.*, "Solar cell efficiency tables (Version 53)," *Prog. Photovoltaics Res. Appl.*, vol. 27, no. 1, pp. 3–12, 2019, doi: 10.1002/pip.3102.

[19] J. Britt and C. Ferekides, "Thin-film CdS/CdTe solar cell with 15.8% efficiency," *Appl. Phys. Lett.*, vol. 62, no. 22, pp. 2851–2852, 1993, doi: 10.1063/1.109629.

[20] H. W. Schock, "Thin film photovoltaics," *Appl. Surf. Sci.*, vol. 92, pp. 606–616, 1996, doi: 10.1016/0169-4332(95)00303-7.

[21] S. B. K. Moorthy, *Thin film structures in energy applications*. Springer, 2015.

[22] K. Rakesh Tej Kumar, M. Ramakrishna, and G. Durga Sukumar, "A review on PV cells and nanocomposite-coated PV systems," *Int. J. Energy Res.*, vol. 42, no. 7, pp. 2305–2319, 2018, doi: 10.1002/er.4002.

[23] C. Klein *et al.*, "Engineering of a novel ruthenium sensitizer and its application in dye-sensitized solar cells for conversion of sunlight into electricity," *Inorg. Chem.*, vol. 44, no. 2, pp. 178–180, 2005, doi: 10.1021/ic048810p.

[24] R. Kavitha and L. G. Devi, "Synergistic effect between carbon dopant in titania lattice and surface carbonaceous species for enhancing the visible light photocatalysis," *J. Environ. Chem. Eng.*, vol. 2, no. 2, pp. 857–867, 2014, doi: 10.1016/j.jece.2014.02.016.

[25] Z. Sen, "SOLAR IRRADIATION FUNDAMENTALS," *Sol. ENERGY Convers. PHOTOENERGY Syst.*, vol. 2, 2007.

[26] R. J. Ellingson *et al.*, "Highly efficient multiple exciton generation in colloidal PbSe and PbS quantum dots," *Nano Lett.*, vol. 5, no. 5, pp. 865–871, 2005, doi: 10.1021/nl0502672.

[27] K. Tvrdy and P. V. Kamat, "Quantum Dot Solar Cells," *Compr. Nanosci. Technol.*, vol.

1–5, pp. 257–275, 2011, doi: 10.1016/B978-0-12-374396-1.00129-X.

[28] C. W. Jiang and M. A. Green, "Silicon quantum dot superlattices: Modeling of energy bands, densities of states, and mobilities for silicon tandem solar cell applications," *J. Appl. Phys.*, vol. 99, no. 11, 2006, doi: 10.1063/1.2203394.

[29] Z. Wang, L. Sun, Y. Ni, L. Liu, and W. Xu, "Flexible Electronics and Healthcare Applications," *Front. Nanotechnol.*, vol. 3, no. March, pp. 1–16, 2021, doi: 10.3389/fnano.2021.625989.

[30] B. Salhi, "Nanowires : Synthesis , Applications and Challenges," *Open Access J. Biosens. Renew. sources*, vol. 1, no. 3, pp. 53–71, 2020.

[31] P. Lee *et al.*, "Highly stretchable and highly conductive metal electrode by very long metal nanowire percolation network," *Adv. Mater.*, vol. 24, no. 25, pp. 3326–3332, 2012, doi: 10.1002/adma.201200359.

[32] Z. Chen, W. Ren, L. Gao, B. Liu, S. Pei, and H. M. Cheng, "Three-dimensional flexible and conductive interconnected graphene networks grown by chemical vapour deposition," *Nat. Mater.*, vol. 10, no. 6, pp. 424–428, 2011, doi: 10.1038/nmat3001.

[33] D. J. Lipomi *et al.*, "Skin-like pressure and strain sensors based on transparent elastic films of carbon nanotubes," *Nat. Nanotechnol.*, vol. 6, no. 12, pp. 788–792, 2011, doi: 10.1038/nnano.2011.184.

[34] L. Groenendaal, F. Jonas, D. Freitag, H. Pielartzik, and J. R. Reynolds, "Poly(3,4-ethylenedioxythiophene) and its derivatives: past, present, and future," *Adv. Mater.*, vol. 12, no. 7, pp. 481–494, 2000, doi: 10.1002/(SICI)1521-4095(200004)12:7<481::AID-

ADMA481>3.0.CO;2-C.

[35] C. N. R. Ã. Rao, F. L. Deepak, G. Gundiah, and A. Govindaraj, "Inorganic nanowires," *Prog. Solid State Chem.*, vol. 31, pp. 5–147, 2003, doi: 10.1016/j.progsolidstchem.2003.08.001.

[36] A. Marti, J. L. Balenzategui, and R. F. Reyna, "Photon recycling and Shockley's diode equation," 1997.

[37] R. F. Pierret, *Semiconductor Device Fundamentals*. Addison-Wesley Publishing Company, 1996.

[38] O. Z. Sharaf and M. F. Orhan, "Concentrated photovoltaic thermal (CPVT) solar collector systems: Part I--Fundamentals, design considerations and current technologies," *Renew. Sustain. Energy Rev.*, vol. 50, pp. 1500–1565, 2015.

[39] D. Muñoz, T. Desrues, and P.-J. Ribeyron, "a-Si: H/c-Si heterojunction solar cells: a smart choice for high efficiency solar cells," *Phys. Technol. Amorph. Heterostruct. Silicon Sol. Cells*, pp. 539–572, 2012.

[40] J. L. Gray, *The Physics of the Solar Cell*. 2011.

[41] C. Kittel, *Introduction to solid state physics*, Eighth., vol. 6, no. 1. John Wiley & Sons, Inc, 2005.

[42] S. M. Sze, *Book Review: Semiconductor Devices Physics and Technology*, 2nd ed., vol. 23, no. 1. John Wiley & Sons, Inc, 2008.

[43] V. Coropceanu, J. Cornil, D. A. da S. Filho, Y. Olivier, Ro. Silbey, and J.-L. Bredas, "Charge transport in organic semiconductors," *Chem. Rev.*, vol. 107, no. 4, 2007, doi:

10.1007/128_2011_218.

[44] G. Malliaras and R. Friend, "An organic electronics primer," *Phys. Today*, vol. 58, no. 5, pp. 53–58, 2005, doi: 10.1063/1.1995748.

[45] C. Deibel and V. Dyakonov, "Polymer-fullerene bulk heterojunction solar cells," *Reports Prog. Phys.*, vol. 73, no. 9, 2010, doi: 10.1088/0034-4885/73/9/096401.

[46] A. N. Sokolov *et al.*, "From computational discovery to experimental characterization of a high hole mobility organic crystal," *Nat. Commun.*, vol. 2, no. 1, 2011, doi: 10.1038/ncomms1451.

[47] J. Nelson, "Diffusion-limited recombination in polymer-fullerene blends and its influence on photocurrent collection," *Phys. Rev. B - Condens. Matter Mater. Phys.*, vol. 67, no. 15, pp. 1–10, 2003, doi: 10.1103/PhysRevB.67.155209.

[48] H. Scher, "Time scale invariance in transport and relaxation," *AIP Conf. Proc.*, vol. 485, 1992, doi: 10.1063/1.42416.

[49] A. M. Carlo, S. Study, and H. Bassler, "Charge Transport in Disordered Organic Photoconductors," vol. 15, 1993.

[50] A. Tyukhova, M. Dentz, W. Kinzelbach, and M. Willmann, "Mechanisms of anomalous dispersion in flow through heterogeneous porous media," vol. 074002, pp. 1–18, 2016, doi: 10.1103/PhysRevFluids.1.074002.

[51] H. Scher and E. W. Montroll, "Anomalous transit-time dispersion in amorphous solids Harvey," *Phys. Rev. B*, vol. 12, 1975.

[52] C. Lee, B. Cobb, L. Ferlauto, and A. Dodabalapur, "Charge carrier velocity distributions

in field-effect transistors," pp. 2–5, 2011, doi: 10.1063/1.3558910.

[53] T. Ha, P. Sonar, A. Dodabalapur, T. Ha, P. Sonar, and A. Dodabalapur, "Charge carrier velocity distributions in high mobility polymer field-effect transistors," vol. 153302, pp. 1–5, 2012, doi: 10.1063/1.3697994.

[54] G. Juška, N. Nekrašas, and K. Genevičius, "Investigation of charge carriers transport from extraction current transients of injected charge carriers," *J. Non. Cryst. Solids*, vol. 358, no. 4, pp. 748–750, 2012, doi: 10.1016/j.jnoncrysol.2011.12.016.

[55] A. Baumann, J. Lorrmann, D. Rauh, C. Deibel, and V. Dyakonov, "A new approach for probing the mobility and lifetime of photogenerated charge carriers in organic solar cells under real operating conditions," *Adv. Mater.*, vol. 24, no. 32, pp. 4381–4386, 2012, doi: 10.1002/adma.201200874.

[56] J. Singh *et al.*, "Effect of temperature on carrier transport and photoconductivity of Mn-doped FeS2 thin films," *Prog. Nat. Sci. Mater. Int.*, vol. 32, no. 1, pp. 135–142, 2022, doi: 10.1016/j.pnsc.2021.10.007.

[57] Y. S. Ju and K. E. Goodson, "Phonon scattering in silicon films with thickness of order 100 nm," *Appl. Phys. Lett.*, vol. 74, no. 20, pp. 3005–3007, 1999, doi: 10.1063/1.123994.

[58] J. Ristein, "Surface Transfer Doping of Semiconductors," *Science (80-.).*, vol. 313, no. August, pp. 1057–1058, 2006.

[59] F. Xiu, J. Xu, P. C. Joshi, C. A. Bridges, and M. P. Paranthaman, "Semiconductor materials for solar photovoltaic cells," in *Semiconductor Materials for Solar Photovoltaic Cells*, 2015, pp. 1–275.

[60] P. Verlinden, "Doping, Diffusion, and Defects in Solar Cells," in *Photovoltaic Solar Energy*, 2017, pp. 21–31.

[61] N. W. Ashcroft and D. N. Mermin, *Solid state physics*, vol. 18, no. 9. Harcourt College Publishers, 1975.

[62] D. M. Nenno, S. Kaltenborn, and H. C. Schneider, "Boltzmann transport calculation of collinear spin transport on short timescales," *Phys. Rev. B*, vol. 94, no. 11, pp. 1–7, 2016, doi: 10.1103/PhysRevB.94.115102.

[63] X. Lu, Y. Sun, and W. Hu, "The external electric field effect on the charge transport performance of organic semiconductors: a theoretical investigation," *J. Mater. Chem. A*, vol. 9, no. 37, pp. 21044–21050, 2021.

[64] R. Enderlein and N. J. M. Horing, *Fundamentals of semiconductor physics and devices*. World Scientific, 1997.

[65] B. G. Bagley, "THE FIELD DEPENDENT MOBILITY OF LOCALIZED ELECTRONIC CARRIERS," *Solid State Commun.*, vol. 8, no. 2, pp. 345–348, 1970.

[66] J. M. Zuo, "Measurements of electron densities in solids: a real-space view of electronic structure and bonding in inorganic crystals," *Reports Prog. Phys.*, vol. 67, no. 11, p. 2053, 2004.

[67] L. H. Thomas, "The calculation of atomic fields," *Math. Proc. Cambridge Philos. Soc.*, vol. 23, no. 5, pp. 542–548, 1927, doi: 10.1017/S0305004100011683.

[68] E. Fermi, "Eine statistische Methode zur Bestimmung einiger Eigenschaften des Atoms und ihre Anwendung auf die Theorie des periodischen Systems der Elemente," *Zeitschrift*

für Phys., vol. 48, no. 1–2, pp. 73–79, 1928, doi: 10.1007/BF01351576.

[69] P. Hohenberg and W. Kohn, "Inhomogeneous Electron Gas," *Phys. Rev.*, vol. 136 (3B), p. 864, 1964, doi: 10.1007/BF01198136.

[70] C. Di Valentin, S. Botti, and M. Cococcioni, *First Principles Approaches to Spectroscopic Properties of Complex Materials*, vol. 347. Springer, 2014.

[71] R. O. Jones, "Density functional theory: Its origins, rise to prominence, and future," *Rev. Mod. Phys.*, vol. 87, no. 3, 2015, doi: 10.1103/RevModPhys.87.897.

[72] W. Kohn and L. J. Sham, "Self-Consistent Equations Including Exchange and Correlation Effects," *Phys. Rev.*, vol. 140(4A), 1965.

[73] A. V. Krukau, O. A. Vydrov, A. F. Izmaylov, and G. E. Scuseria, "Influence of the exchange screening parameter on the performance of screened hybrid functionals," *J. Chem. Phys.*, vol. 125, no. 22, 2006, doi: 10.1063/1.2404663.

[74] J. P. Perdew, M. Ernzerhof, and K. Burke, "Rationale for mixing exact exchange with density functional approximations," *J. Chem. Phys.*, vol. 105, no. 22, pp. 9982–9985, 1996, doi: 10.1063/1.472933.

[75] H. P. Komsa and A. Pasquarello, "Assessing the accuracy of hybrid functionals in the determination of defect levels: Application to the As antisite in GaAs," *Phys. Rev. B - Condens. Matter Mater. Phys.*, vol. 84, no. 7, pp. 1–6, 2011, doi: 10.1103/PhysRevB.84.075207.

[76] E. H. Lieb, "Two theorems on the Hubbard model," *Phys. Rev. Lett.*, vol. 62, no. 10, pp. 1201–1204, 1989, doi: 10.1103/PhysRevLett.62.1201.

[77] N. Marzari, A. A. Mostofi, J. R. Yates, I. Souza, and D. Vanderbilt, "Maximally localized Wannier functions: Theory and applications," *Rev. Mod. Phys.*, vol. 84, no. 4, pp. 1419–1475, 2012, doi: 10.1103/RevModPhys.84.1419.

[78] R. Zimmermann *et al.*, "Electronic structure of 3d-transition-metal oxides: On-site Coulomb repulsion versus covalency," *J. Phys. Condens. Matter*, vol. 11, no. 7, pp. 1657–1682, 1999, doi: 10.1088/0953-8984/11/7/002.

[79] H. J. Kulik, M. Cococcioni, D. A. Scherlis, and N. Marzari, "Density functional theory in transition-metal chemistry: A self-consistent hubbard U approach," *Phys. Rev. Lett.*, vol. 97, no. 10, pp. 1–4, 2006, doi: 10.1103/PhysRevLett.97.103001.

[80] J. A. Anta *et al.*, "Continuity Equation for the Simulation of the Current-Voltage Curve and the Time-Dependent Properties in Dye-Sensitized Solar Cells," *Phys. Chem. Chem. Phys.*, pp. 1–33, 2012.

[81] R. Katoh *et al.*, "Charge Generation and Recombination in Diketopyrrolopyrrole Polymer: Fullerene Bulk Heterojunctions Studied by Transient Absorption and Time-Resolved Microwave Conductivity," *J. Phys. Chem. C*, vol. 120, no. 50, pp. 28398–28406, 2016.

[82] D. D. O'Regan, *Optimised projections for the ab initio simulation of large and strongly correlated systems*. Springer Science \& Business Media, 2011.

[83] G. A. Hallock and M. A. Meier, "Low frequency pressure modulation of indium antimonide," *Rev. Sci. Instrum.*, vol. 073906, pp. 1–10, 2012.

[84] H. Salehi Najafabadi, M. A. Meier, and G. A. Hallock, "Charge carrier transport and electrical response by driving band gap modulation in semiconductors," *Appl. Mater.*

Today, vol. 29, no. August, p. 101608, 2022, doi: 10.1016/j.apmt.2022.101608.

[85] N. Kausar, B. ul Islam, S. A. Ahmad, and M. A. Waqar, "Intuitionistic Fuzzy Ideals with Thresholds (Î$\pm$, Î^2] in LA-rings," *Eur. J. Pure Appl. Math.*, vol. 12, no. 3, pp. 906–943, 2019.

[86] P. Giannozzi *et al.*, "Advanced capabilities for materials modelling with Quantum ESPRESSO," *J. Phys. Condens. Matter*, vol. 29, no. 46, 2017, doi: 10.1088/1361-648X/aa8f79.

[87] P. Giannozzi *et al.*, "QUANTUM ESPRESSO: A modular and open-source software project for quantum simulations of materials," *J. Phys. Condens. Matter*, vol. 21, no. 39, 2009, doi: 10.1088/0953-8984/21/39/395502.

[88] M. Gajdoš and J. Hafner, "CO adsorption on Cu (1 1 1) and Cu (0 0 1) surfaces: Improving site preference in DFT calculations," *Surf. Sci.*, vol. 590, no. 2–3, pp. 117–126, 2005.

[89] S. Atahan-Evrenk and A. Aspuru-Guzik, "Prediction and calculation of crystal structures," *Top. Curr. Chem.*, vol. 345, 2014.

[90] Y. Watanabe, "Microscopic derivation of free energy under electric field in ferroelectric and ferroelectric heterostructures containing free carriers," *Ferroelectrics*, vol. 333, no. 1, pp. 57–67, 2006.

[91] J. Navas *et al.*, "Direct estimation of the electron diffusion length in dye-sensitized solar cells," *J. Phys. Chem. Lett.*, vol. 2, no. 9, pp. 1045–1050, 2011.

[92] M. Burgelman, P. Nollet, and S. Degrave, "Modelling polycrystalline semiconductor solar

cells," *Thin Solid Films*, vol. 361, pp. 527–532, 2000, doi: 10.1016/S0040-6090(99)00825-1.

[93] S. Khelifi *et al.*, "Effect of light induced degradation on electrical transport and charge extraction in polythiophene:Fullerene (P3HT:PCBM) solar cells," *Sol. Energy Mater. Sol. Cells*, vol. 120, no. PART A, pp. 244–252, 2014, doi: 10.1016/j.solmat.2013.09.010.

[94] M. S. Chowdhury *et al.*, "Effect of deep-level defect density of the absorber layer and n/i interface in perovskite solar cells by SCAPS-1D," *Results Phys.*, vol. 16, 2019, doi: 10.1016/j.rinp.2019.102839.

[95] T. R. Lenka, A. C. Soibam, K. Dey, T. Maung, and F. Lin, "Numerical analysis of high-efficiency lead-free perovskite solar cell with NiO as hole transport material and PCBM as electron transport material," *CSI Trans. ICT*, 2020, doi: 10.1007/s40012-020-00291-7.

[96] A. Slami, M. Bouchaour, and L. Merad, "Numerical Study of Based Perovskite Solar Cells by SCAPS-1D," *Int. J. Energy Environ.*, vol. 13, no. December, pp. 17–21, 2019.

[97] L. A. Agapito, S. Curtarolo, and M. B. Nardelli, "Reformulation of DFT+ U as a pseudohybrid hubbard density functional for accelerated materials discovery," *Phys. Rev. X*, vol. 5, no. 1, p. 11006, 2015.

[98] Z. Huang and D. Zhang, "Bandgap engineering of PbTe ultra-thin layers by surface passivations," *J. Phys. Condens. Matter*, vol. 31, no. 29, p. 295503, 2019.

[99] C. B. Carter and M. G. Norton, *Ceramic materials: science and engineering*, vol. 716. Springer, 2007.

[100] S. Hüfner, "Electronic structure of NiO and related 3d-transition-metal compounds," *Adv.*

Phys., vol. 43, no. 2, pp. 183–365, 1994.

[101] D. I. Castelhano, J. de Almeida, C. H. de Paiva Pinheiro, R. Bertazzoli, and C. de Arruda Rodrigues, "Array of electrodeposited Ru-decorated TiO 2 nanotubes with enhanced photoresponse," *J. Solid State Electrochem.*, vol. 22, pp. 2445–2455, 2018.

[102] Y. Zhang, "Thermal oxidation fabrication of NiO film for optoelectronic devices," *Appl. Surf. Sci.*, vol. 344, pp. 33–37, 2015.

[103] J. Asare *et al.*, "A hybrid hole transport layer for perovskite-based solar cells," *Energies*, vol. 14, no. 7, pp. 1–13, 2021, doi: 10.3390/en14071949.

[104] T. A. Atesin, S. Bashir, and J. L. Liu, *Nanostructured Materials for Next-Generation Energy Storage and Conversion*. Springer, 2017.